

Magnetic fields in barred galaxies.

IV. NGC 1097 and NGC 1365

R. Beck¹, A. Fletcher^{1,2}, A. Shukurov², A. Snodin², D. D. Sokoloff³, M. Ehle⁴, D. Moss⁵, V. Shoutenkov⁶

¹ Max-Planck-Institut für Radioastronomie, Auf dem Hügel 69, 53121 Bonn, Germany

² School of Mathematics and Statistics, University of Newcastle, Newcastle upon Tyne NE1 7RU, UK

³ Department of Physics, Moscow State University, 119992 Moscow, Russia

⁴ XMM-Newton Science Operations Centre, European Space Astronomy Centre (ESAC), European Space Agency, P.O. Box 50727, 28080 Madrid, Spain

⁵ School of Mathematics, University of Manchester, Manchester M13 9PL, UK

⁶ Pushchino Radioastronomy Observatory, Astro Space Center, 142292 Pushchino, Russia

Received 2 June 2005 / Accepted 2 August 2005

Abstract. We present $\lambda 3.5$ cm and $\lambda 6.2$ cm radio continuum maps in total and polarized intensity of the barred galaxies NGC 1097 (at $2''$ – $15''$ resolution) and NGC 1365 (at $9''$ – $25''$ resolution). A previously unknown radio galaxy southwest of NGC 1097 is reported. Apart from a smooth faint envelope and a bright central region, both galaxies exhibit radio ridges roughly overlapping with the massive dust lanes in the bar region. The contrast in total intensity across the radio ridges is compatible with compression and shear of an isotropic random magnetic field, where the gas density compression ratio is approximately equal to 4 and the cosmic ray density is constant across the ridges. The contrast in polarized intensity is significantly smaller than that expected from compression and shearing of the regular magnetic field; this could be the result of decoupling of the regular field from the dense molecular clouds. The regular field in the ridge is probably strong enough to reduce significantly shear in the diffuse gas (to which it is coupled) and hence to reduce magnetic field amplification by shearing. This contributes to the misalignment of the observed field orientation with respect to the velocity vectors of the dense gas. Our observations, for the first time, indicate that *magnetic forces can control the flow of the diffuse interstellar gas at kiloparsec scales*. The total radio intensity reaches its maximum in the circumnuclear starburst regions, where the equipartition field strength is about $60 \mu\text{G}$, amongst the strongest fields detected in spiral galaxies so far. The regular field in the inner region has a spiral shape with large pitch angle, indicating the action of a dynamo. Magnetic stress leads to mass inflow towards the centre, sufficient to feed the active nucleus in NGC 1097. – We detected diffuse X-ray emission, possibly forming a halo of hot gas around NGC 1097.

Key words. galaxies: magnetic fields – galaxies: individual: NGC 1097, NGC 1365 – galaxies: nuclei – galaxies: spiral – galaxies: bars – galaxies: structure – ISM: magnetic fields

1. Introduction

Radio polarization observations have revealed basic properties of interstellar magnetic fields in galaxies of various morphological types (Beck et al. 1996; Beck 2005). Until recently magnetic fields in barred galaxies remained relatively unexplored, although they can be expected to have interesting properties. Strong non-axisymmetric gas flows and large-scale shocks will have a major effect on interstellar magnetic fields; velocity gradients may enhance the regular magnetic field (Chiba & Lesch 1994, Otmianowska-Mazur et al. 1997) and dynamo action should also be strongly affected by the presence of a bar (Moss et al. 1998). According to gas-dynamical simulations, a shear shock occurs in the bar where the gas

streamlines are deflected inwards (Athanassoula 1992a, 1992b; Piner et al. 1995). To date, none of the numerical models includes the magnetic field in a way that allows its influence on the shock to be explored, although it is well known that magnetized shocks can develop properties different from those of hydrodynamic shocks.

Radio observations of barred galaxies can then provide useful insight into their interstellar gas dynamics. In order to clarify the nonthermal properties of barred galaxies, we have performed a radio survey of a sample of barred galaxies (Beck et al. 2002). Among the twenty galaxies studied, the prototypical examples NGC 1097 and NGC 1365 are most spectacular. Here we discuss in detail and interpret, in terms of gas flow and magnetic field models, the non-thermal properties of these two galaxies.

The total [polarized + unpolarized] synchrotron radio intensity depends on the strength of the total [regular + random] magnetic field in the sky plane and the energy density of cosmic ray electrons. Polarized synchrotron emission is produced by cosmic ray electrons in the presence of either a regular (coherent) magnetic field ¹, or an anisotropic random (incoherent) field, or a combination of both. Faraday rotation is produced by the component of the regular field along the line of sight and thermal electrons. Since the polarization angle is only sensitive to the orientation of the magnetic field in the synchrotron source (rather than to its direction), only Faraday rotation is sensitive to the distinction between regular and random anisotropic magnetic fields. The anisotropy of the random interstellar magnetic field can be significant in barred galaxies where it is produced by strong shear and shocks. Therefore, the magnetic field strength obtained from polarized intensity, ² denoted here B_P , must be carefully distinguished from that of the regular magnetic field \overline{B} . Denoting the strength of the anisotropic part of the random magnetic field (\mathbf{b}) by b_a , we can write $B_P^2 = \overline{B}^2 + \overline{b_a^2}$.

The first high-resolution radio map of a barred galaxy, NGC 1097 (Ondrechen & van der Hulst 1983), showed narrow radio ridges coinciding with the dust lanes, the tracers of compression regions along the leading edge of the bar. A similar result was obtained for M83 (Ondrechen 1985), a galaxy with a smaller bar than NGC 1097. The first detection of polarized radio emission from a bar was reported by Ondrechen (1985) for M83, with a mean fractional polarization of 25%.

The first high-resolution polarization observations of a galaxy with a massive bar, NGC 1097, by Beck et al. (1999) had a resolution of 15''. Magnetic field orientations in and around the bar were shown to approximately follow the velocity field of the gas in the corotating frame, while the outer field has a spiral pattern. A narrow ridge of vanishing polarized intensity indicated deflection of the field lines in a shear shock, similar to the deflection of the velocity vectors (Athanasoula 1992b).

Moss et al. (2001) presented a generic dynamo model, based on the model velocity field of Athanasoula (1992b), which could explain the major magnetic features observed in radio polarization. A similar dynamo model, but now based on the specific velocity and gas density fields of NGC 1365, is discussed by Moss et al. (2005). Beck et al. (2002) presented an atlas of radio maps (in total and polarized intensity) of northern and southern barred galaxies observed with the VLA and the ATCA at a resolution of

30''. Harnett et al. (2004) discussed ATCA radio observations of the peculiar barred galaxy NGC 2442. The circumnuclear rings of the southern barred galaxies NGC 1672 and NGC 7552 were discussed by Beck et al. (2005).

In this paper, we present VLA observations of NGC 1097 and NGC 1365, with higher resolution than in Beck et al. (1999) and Beck et al. (2002), which resolve the structure of the magnetic field in the ridges of NGC 1097 and NGC 1365 and in the circumnuclear starburst regions. Furthermore, we present a ROSAT X-ray map of NGC 1097.

NGC 1097 is a barred galaxy of morphological type SBb(s) at about 17 Mpc distance ($1'' \approx 83$ pc), with a bar of about 20 kpc in length continuing into two optical spiral arms. The galaxy plane is inclined by about 45° to the line of sight, and its line of nodes has a position angle of about -45° with respect to the north-south direction (Ondrechen et al. 1989), with the south-western side closer to us. The bar has a similar position angle of about -32° and thus lies almost in the plane of the sky. In the galaxy's plane, the bar is located at $\simeq 18^\circ$ azimuthal angle from the major axis. Very little H I gas has been found in the bar (Ondrechen et al. 1989). CO observations by Gerin et al. (1988) were not sensitive enough to detect cold gas in the bar. Crosthwaite (2001) detected extended CO emission in the (1-0) and (2-1) transitions, but the spatial resolution was insufficient to see any gas compression in the bar. Roussel et al. (2001) imaged NGC 1097 and NGC 1365 in the mid-infrared. Dust emission is relatively weak in the bar's ridge, and substantial diffuse emission was detected around the bar.

The nuclear ring of 18'' (1.5 kpc) diameter, formed by accreting gas, shows enhanced star formation. This conspicuous feature is visible in the optical, CO, radio continuum and X-ray spectral ranges. Some spiral dust filaments were discovered interior to the ring (Barth et al. 1995, Prieto et al. 2005), possibly indicating mass inflow towards the active nucleus.

NGC 1097A is a companion dwarf galaxy at about 18 kpc projected distance towards the north-west (see Fig. 3), which causes gravitational distortions in the northern half of NGC 1097 and a tidal arm in the H I gas (Ondrechen et al. 1989).

NGC 1365, at 18.6 Mpc distance ($1'' \approx 93$ pc), is probably the best studied barred galaxy (see the review by Lindblad 1999). The H I emission and velocity field have been studied in detail by Ondrechen & van der Hulst (1989) and Jörsäter & van Moorsel (1995). The galaxy plane is inclined by about 40° to the line of sight and its line of nodes has a position angle of about 40° with respect to the north-south direction. The north-western side is closer to the observer. The bar has a length of about 22 kpc and a position angle of about 92°.

NGC 1365 has an active Seyfert nucleus like NGC 1097, but the circumnuclear ring in radio continuum is incomplete (Sandqvist et al. 1995). Radio continuum emission from the bar has first been detected by Beck et al. (2002), it coincides with the dust lanes, as in NGC 1097.

¹ The regular field is also known as the mean, average, ordered, or large-scale field, but these terms could be misleading and are avoided in this paper.

² In observational papers it is generally stated that the polarized emission is a signature of the regular field, without defining the term 'regular'. In many papers the possible contribution of the anisotropic random field to the polarized emission is neglected. Our definition is such that only *coherent* fields are called regular.

The map of NGC 1365 at $\lambda 3.5$ cm with $30''$ resolution (Beck et al. 2002, their Fig. 7) shows a deflection of the regular magnetic field in its eastern bar, though smoother than in NGC 1097. Data at higher resolution and corrected for Faraday rotation are presented in this paper (Sect. 3.4).

2. Observations

2.1. Radio observations

NGC 1097 and NGC 1365 were observed with the Very Large Array (VLA) operated by the NRAO³ in its DnC and CnB arrays at 4.86 GHz ($\lambda 6.2$ cm) and 8.46 GHz ($\lambda 3.5$ cm). At both frequencies two IFs, separated by 50 MHz and with a bandwidth of 50 MHz each, were recorded. 3C48 and 3C138 were used as primary flux calibrators, 3C138 was also used for polarization angle calibration; 0240-231 was our phase calibrator. Details of the observations are given in Table 1.

Data processing was done with the standard procedures of AIPS. Visibility data in the same frequency band, obtained from the different observation periods, from the different arrays and from both IF channels, were combined in the uv plane. Maps in Stokes parameters I , Q and U were obtained by IMAGR from the combined data at each frequency band. Different weightings were applied to obtain maps with different resolutions (Table 2). Uniform weighting (which gives the same weights to each cell in the uv plane) reveals the best angular resolution, but larger r.m.s. noise than ‘natural’ weighting (which gives the same weights to all antenna pairs and hence emphasizes the inner uv plane) or ‘robust’ weighting (an intermediate case).

At both wavelengths, several values of the ‘zero-spacing’ flux and its weight were tested in the IMAGR cleaning process to minimize the negative-bowl effect in the total-intensity images caused by missing short-baseline visibility data in the uv plane.

The largest structures visible to the VLA D-array are about $3'$ at $\lambda 3.5$ cm and $5'$ at $\lambda 6.2$ cm, less than the full extent of the galaxies as observed at $\lambda 20$ cm (Beck et al. 2002). No single-dish maps are available to add the missing large-scale emission component in total intensity. Hence our maps can only be used for spectral index studies of the bright ridges and central regions (Figs. 7 and 9). We do not expect that any large-scale structure is missing in the maps of the Stokes parameters Q and U (and, hence, in the polarized intensity maps) because the magnetic field orientation and hence the polarization angle is not constant across the galaxies.

Maps of the linearly polarized intensity (P) and the polarization angle (PA) were obtained from the Q and U maps. The positive bias in P due to noise was subtracted by applying the POLCO correction.

The final maps of NGC 1097 were smoothed to circular FWHM Gaussian beams of $2''$ (central region, Fig. 14), $4''$ (Figs. 8 and 14), $6''$, $10''$ and $15''$ (Figs. 1–3). Polarization angles at $10''$ resolution were used to compute the map of Faraday rotation (Fig. 11).

For NGC 1365, no data with the CnB array were obtained, so that the highest achievable resolution (uniform weighting) is $7''$ at $\lambda 3.5$ cm and $13''$ at $\lambda 6.2$ cm. However, the maps at these resolutions have low signal-to-noise ratios and show little extended emission. In this paper, we present only maps obtained with robust and natural weighting (see Table 2). Diffuse emission of NGC 1365 is best visible in the maps at $15''$ resolution (Fig. 4) and especially in the $\lambda 6.2$ cm maps at $25''$ resolution (Fig. 5). Maps of the central region at $9''$ resolution are shown in Fig. 15. Polarization angles at $25''$ resolution were used to compute the map of Faraday rotation (Fig. 11).

The total intensity maps of NGC 1365 were corrected for primary beam attenuation. This correction was not necessary for the total intensity maps of NGC 1097 and the polarization maps of both galaxies because the extent of the visible emission is smaller than the diameter of the primary beam ($5.4'$ at $\lambda 3.5$ cm and $9'$ at $\lambda 6.2$ cm). However, the spectral index is sensitive to small systematic effects, and thus the total intensity of NGC 1097 used for the maps of spectral index (Figs. 7 and 9) had to be corrected for primary beam attenuation.

The values for resolution and r.m.s. noise of the maps shown in this paper are given in Table 2.

2.2. X-ray observations of NGC 1097

NGC 1097 was observed on Dec 27, 1992, for 2.7 hours with the Position Sensitive Proportional Counter (PSPC, Pfeffermann et al. 1987) on board the *ROSAT* X-ray satellite (observation request 600449, PI: H. Arp). We retrieved the data from the ROSAT Data Archive and performed a standard spatial and spectral analysis with the Extended X-ray Scientific Analysis System (EXSAS, Zimmermann et al. 1998).

To show the extended soft-band X-ray emission, the data was spatially binned, exposure corrected and smoothed in energy sub-bands (cf. Ehle et al. 1998). The smoothing was done with a Gaussian filter with the FWHM corresponding to the average resolution of the point spread function at the PSPC centre in the individual energy sub-bands. The two lowest sub-bands (0.11–0.19 keV and 0.20–0.41 keV), smoothed to $52''$ and $38''$ resolutions, respectively, were added to create a standard soft-band (0.1–0.4 keV) map of the X-ray emission of NGC 1097 (Fig. 16).

The spatial distribution and spectral characteristics of the soft X-ray emission are discussed in Sect. 6.

³ The NRAO is a facility of the National Science Foundation operated under cooperative agreement by Associated Universities, Inc.

Table 1. Observational parameters of VLA observations

	NGC 1097	NGC 1365
Frequency (GHz)	4.835 & 4.885	4.835 & 4.885
Array	DnC	DnC
Pointing (J2000)	02 ^h 46 ^m 19 ^s .77–30° 16′28″.55	03 ^h 33 ^m 35 ^s .50–36° 07′59″.88
Observing date	1996 May 20	1996 May 20 and 1999 Feb 19
Net observing time (min)	32	20 and 280
Shortest baseline	506λ	490λ and 404λ
Frequency (GHz)	4.835 & 4.885	
Array	CnB	
Pointing (J2000)	02 ^h 46 ^m 19 ^s .87–30° 16′27″.30	
Observing date	1998 Nov 13 & 15	
Net observing time (min)	560	
Shortest baseline	765λ	
Frequency (GHz)	8.435 & 8.485	8.435 & 8.485
Array	DnC	DnC
Pointing (J2000)	02 ^h 46 ^m 19 ^s .81–30° 16′28″.05	03 ^h 33 ^m 35 ^s .50–36° 07′59″.88
Observing date	1996 May 20 and 1997 Oct 07 & 09	1996 May 20 and 1997 Oct 07 & 09
Net observing time (min)	38 and 312	24 and 311
Shortest baseline	794λ and 704λ	790λ and 704λ
Frequency (GHz)	8.435 & 8.485	
Array	CnB	
Pointing (J2000)	02 ^h 46 ^m 19 ^s .87–30° 16′27″.30	
Observing date	1998 Nov 11 & 14	
Net observing time (min)	560	
Shortest baseline	1330λ	

Table 2. Weights and r.m.s. noise values of total intensity σ_I and of polarized intensity $\sigma_{Q,U}$ (for Stokes parameters Q and U) (in $\mu\text{Jy}/\text{beam}$) in the final maps

	NGC 1097					NGC 1365		
Beam size	2″	4″	6″	10″	15″	9″	15″	25″
$\lambda 3.5 \text{ cm}$								
Weighting	uniform	robust	natural	natural	natural	robust	natural	natural
σ_I	9	7	8	11	17	12	12	20
$\sigma_{Q,U}$	9	7	6	8	11	12	12	15
$\lambda 6.2 \text{ cm}$								
Weighting	–	uniform	natural	natural	natural	–	robust	natural
σ_I	–	12	8	15	20	–	14	14
$\sigma_{Q,U}$	–	12	8	9	13	–	14	14

3. The radio maps

3.1. Discovery of a radio galaxy in the field of NGC 1097

A radio galaxy is visible about 90″ southwest of the nucleus of NGC 1097 (Figs. 1 and 6). It is not included in the NED and NVSS catalogues. The position of the nucleus (which is still unresolved at 2″ resolution) is RA, DEC(J2000) = 02 46 12.75, –30 17 05.3, its flux density is $753 \pm 10 \mu\text{Jy}$ at $\lambda 3.5 \text{ cm}$, and its spectrum is flat (with a spectral index $\alpha \simeq +0.1$) which is typical of an active galactic nucleus. The northern component is located at RA, DEC(J2000) = 02 46 12.7, –30 17 01, its flux density is $283 \pm 36 \mu\text{Jy}$ at $\lambda 3.5 \text{ cm}$, and its spectrum is steep ($\alpha \simeq -0.5$). The southern jet shows a spectral steepening from $\alpha \simeq +0.1$ to $\alpha \simeq -1.5$ with increasing distance from

the nucleus. No polarized emission was detected from any component.

3.2. The radio ridges in the bar regions

The total and polarized radio continuum emission of NGC 1097 and NGC 1365 is strongest near the galactic centres (see Sects. 5.1 and 5.2) and in *radio ridges* that approximately coincide with the prominent dust lanes seen in the optical images (Figs. 1–8). The lengths of the ridges are close to the bar lengths. As gas and stars in the bar region rotate faster than the bar pattern in the clockwise direction (Ondrechen et al. 1989), the ridges are located on the ‘downstream’ side of the bar which is *leading* with respect to the sense of rotation, and the regions ‘upstream’ of the shock front are located on the *following* side of

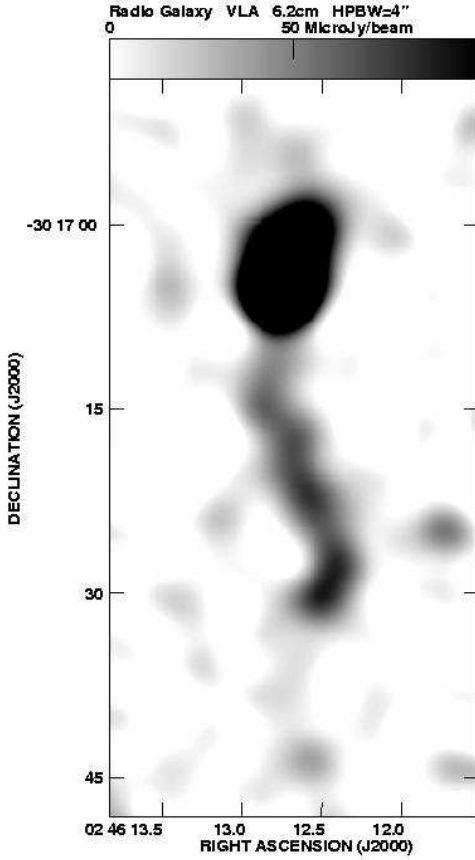


Fig. 6. Radio galaxy west of NGC 1097 (total intensity), observed at $\lambda 6.2$ cm with $4''$ resolution.

the bar. The ridges enter the central region tangentially to the circumference at the two points where the absolute maxima of polarized intensity occur, as can be seen in the lower panels of Figs. 1 and 4. Significant polarized emission P is also detected outside of the ridges in the upstream regions (Figs. 2 and 4) and from around the whole bar region, forming a smooth envelope (Figs. 3 and 5, see Sect. 3.7).

The general properties of the radio ridges, summarized in Table 3, have been determined from the maps at $\lambda 6.2$ cm, with $6''$ (≈ 500 pc) resolution for NGC 1097 and with $15''$ (≈ 1.4 kpc) resolution for NGC 1365.

The *thermal fractions* of the radio emission f_{th} in the ridges were estimated from the observed spectral index (Fig. 7), assuming a constant synchrotron spectral index of $\alpha_s = -1.0$. A synchrotron spectral index of $\alpha_s = -1$ is expected from particle acceleration in strong shocks ($\alpha_0 = -0.5$ intrinsically, steepened by $\Delta\alpha = -0.5$ due to synchrotron and/or inverse Compton losses). We attribute the observed flattening of the spectrum with increasing distance from the centre of NGC 1097 (Table 3) to a larger thermal fraction in the outer parts of the ridge. This is in line with the $\text{H}\alpha$ intensity (Quillen et al. 1995) which is very small in the inner bar and stronger in the middle bar of NGC 1097. In NGC 1365, no similar effect was detected. However, the separation of thermal and

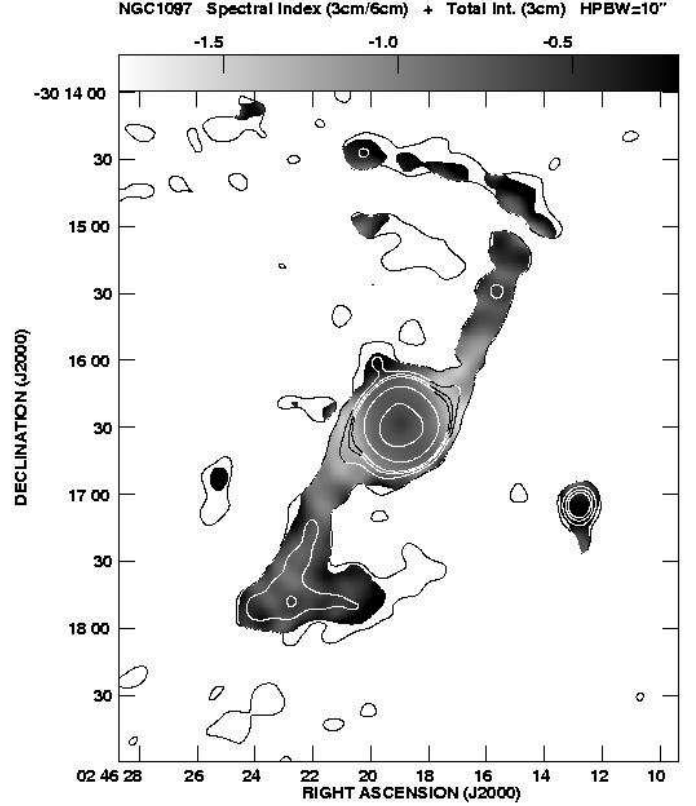


Fig. 7. Spectral index of NGC 1097 between $\lambda 3.5$ cm and $\lambda 6.2$ cm at $10''$ resolution, shown where the signal at each wavelength exceeds $15\sigma_I$ (to avoid systematic effects due to the missing large-scale structures). Contours represent $\lambda 3.5$ cm total intensity at 1, 2, 3, 4, 16, 64 times $150 \mu\text{Jy}/\text{beam}$ area and the same resolution.

nonthermal emissions is uncertain because of the possible error in spectral index due to the uncertainty in α_s , and also due to missing large-scale emission in the total intensity maps. Hence the values for f_{th} in Table 3 should be regarded as crude estimates. For a more detailed study, high-resolution observations at further frequencies or sensitive, extinction-corrected $\text{H}\alpha$ data are required.

At the highest available resolution ($4''$, corresponding to about 330 pc) the southern total-intensity radio ridge of NGC 1097 is resolved into several features (Fig. 8) which are not strictly aligned with the ridge axis, neither do they coincide with the dust clouds visible in the optical image. The strongest peaks are located upstream of the dust lanes, and some of them coincide with star formation regions visible in the optical images. According to the radio spectral index map (Fig. 9) the emission from the peaks is a mixture of thermal and nonthermal components. The observed spectral index α reveals strong variations along the bar, with values ranging between -0.1 (expected for purely thermal emission) and less than -1 (typical of purely nonthermal emission by cosmic-ray electrons suffering from synchrotron energy loss in a strong magnetic field).

The location of the star formation complexes upstream of the radio ridges seems to be in conflict with the picture of the onset of star formation in the shock, as observed in other barred galaxies (Sheth et al. 2002). Our observations indicate that some compression of gas and magnetic fields occurs ahead of the shock front, perhaps in the narrow dust filaments mentioned in Sect. 3.3.

The upstream and downstream regions in P are separated by valleys of low polarized emission, the *depolarization valleys*, which are discussed in Sect. 3.3. The polarized intensities are similar on both sides of the depolarization valleys, whereas the total intensity is much larger on the ridges. Thermal emission cannot account for the enhanced total emission in the ridges (see Table 3). This indicates that mainly the turbulent component of the magnetic field is compressed in the shock, while the regular field remains almost unaffected. This surprising result will be discussed in Sects. 8.1 and 8.2.

In NGC 1097, the *average degree of polarization* p of the synchrotron emission $p = P/I_s$ at $\lambda 6.2$ cm decreases from about 30% in the middle southern ridge to about 5% at the end of the bar (Table 3), while it is almost constant (approximately 20%) along the northern ridge (here I_s is the synchrotron intensity). In NGC 1365, p is low (5–15%) along both ridges. The degrees of polarization are generally similar at $\lambda 3$ cm and $\lambda 6$ cm, indicating that Faraday depolarization is small (see the right-hand panel of Fig. 11), except in the inner ridges and in the central regions. In the region upstream of the ridge p is 30–40% (in both galaxies), larger than in the ridge.

The observed *half-maximum full width* w (in both total and polarized intensity – the difference is insignificant) of the northern and southern ridges of NGC 1097 increases from about 600 pc near the circumnuclear ring to about 900 pc near the end of the bar. Assuming a Gaussian ridge profile, the observed width w was corrected for smearing by the telescope beam (with a Gaussian half-power width Θ) to obtain the intrinsic width w_0 via $w_0^2 = w^2 - \Theta^2$. The intrinsic width varies from about 400 pc to about 700 pc (Table 3). The radio ridges of NGC 1365 are broader and shorter than in NGC 1097, with an intrinsic width of $\simeq 1000$ pc and a length of about 1.5 (8 kpc).

The *total intensity contrast* in NGC 1097 between the ridges and the surrounding regions, at $\pm(7''-12'')$ distance from the ridge axis, is about 10 in the inner ridge and decreases to about 5 towards the bar's end (Table 3). These estimates apply to both the northern and the southern ridges, although the radio emission in the northern ridge is fainter. In NGC 1365, the contrast is about 10 in the eastern and 5 in the western ridge, while the total radio intensity is higher in the west (Table 3).

The *contrast in polarized intensity* between the ridges and their surroundings is quite different from that in total intensity (Table 3). Strong polarized emission is observed upstream of the radio ridge and dust lane in one half of each galaxy (especially to the west of the southern ridge in NGC 1097 and south of the eastern ridge in NGC 1365), separated from the polarization ridge by a narrow ‘depo-

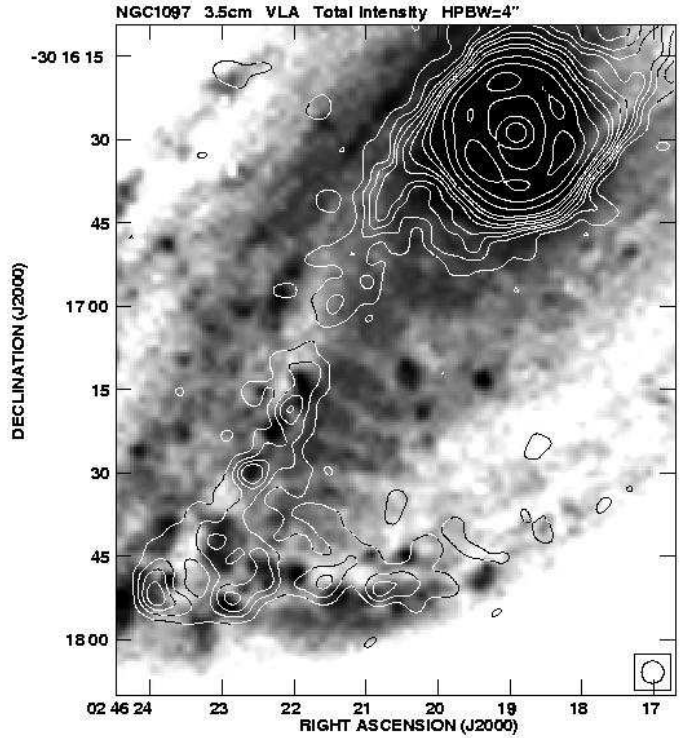


Fig. 8. Total intensity contours of the central and southern parts of NGC 1097 at $\lambda 3.5$ cm at $4''$ resolution. The contour intervals are as in Fig. 1, with the basic contour level at $20 \mu\text{Jy}/\text{beam area}$ (the 3σ level).

larization valley’ (see Sect. 3.3). Near the outer end of the ridges, the polarized intensity upstream is even stronger than in the ridge, so that the contrast is smaller than unity. In the northern and inner southern ridges of NGC 1097, the polarized intensity is about 7 times higher than in the upstream regions. The difference from the total intensity ridges suggests that turbulent and regular magnetic fields respond differently to compression and shear in the dust lane region (see Sect. 8).

The ridge of total intensity observed in NGC 1097 is systematically *shifted* from that in polarized intensity (Fig. 20). As determined from several one-dimensional cuts of the southern ridge at $10''$ resolution, the peak in total intensity is about $5''$ (400 pc) upstream – i.e. to the south-west – compared to the peak in polarized intensity. Note that the position of the peak of an emission structure can be determined with a better accuracy than the beam width if the signal-to-noise ratio is high (Harnett et al. 2004). Figure 2 shows that the polarized intensity follows the optical dust lanes very closely.

In the northern ridge of NGC 1097, a similar shift between the ridges of total and polarized emission is visible, though less clearly due to the weaker polarized emission. In NGC 1365, an offset has not been detected. However, the resolution of our data is lower than for NGC 1097, so that a shift of $\leq 10''$ cannot be excluded.

Table 3. Properties of the radio ridges in the bars of NGC 1097 and NGC 1365 from the $\lambda 6.2$ cm data. I is the total intensity, P the polarized intensity. ϵ_I and ϵ_P are the contrasts in I and P between the ridges and the surrounding regions. α is the spectral index between $\lambda 6.2$ cm and $\lambda 3.5$ cm, f_{th} is the thermal fraction of I , $I_s = I(1 - f_{\text{th}})$ is the synchrotron intensity, and $p = P/I_s$ is the fractional polarization of the synchrotron emission. B_I and B_P are the equipartition strengths of the total and regular + anisotropic random magnetic fields derived from I_s and P (see Sect. 3.6). The distance along the NGC 1097 ridge is measured from the galaxy’s centre. For NGC 1365, average values along the ridges are given.

	Width in I [pc]	Contrast ϵ_I	Width in P [pc]	Contr. ϵ_P	Spectral index α	Thermal fract. f_{th}	Fractional polarization p	B_I [μG]	B_P [μG]
NGC 1097									
Inner ridge (2 kpc south)	400	10	400	7	-1.0	< 0.05	0.10	30	9
Middle ridge (4 kpc south)	500	7	700	1.5	-0.9	0.05	0.28	20	12
Outer ridge (6 kpc south)	700	5	800	0.9	-0.7	0.25	0.15	22	9
NGC 1365									
Eastern ridge	900	10	900	0.5	-0.75	0.2	0.13	24	10
Western ridge	1000	5	900	3	-0.75	0.2	0.04	30	7

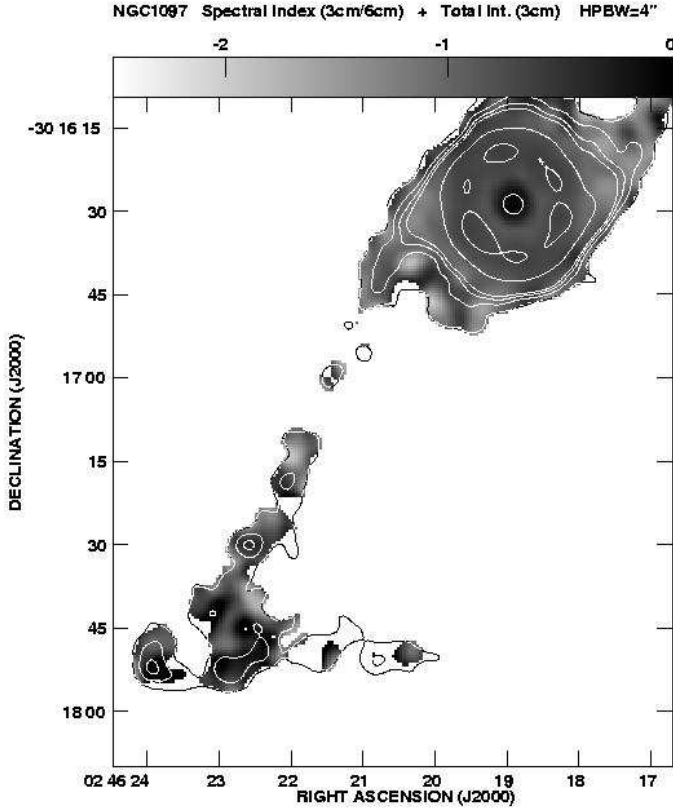


Fig. 9. Spectral index of the central region and southern ridge of NGC 1097 between $\lambda 3.5$ cm and $\lambda 6.2$ cm at $4''$ resolution, shown where the signal exceeds $5\sigma_I$ at each wavelength. Contours show the $\lambda 3.5$ cm total intensity at 1, 2, 3, 4, 16, 64 times $40\mu\text{Jy}/\text{beam area}$ and the same resolution.

3.3. The magnetic field structure in the bar regions

The B -vectors of polarized emission in the bar region change their orientation rapidly upstream of the dust lanes in both galaxies (Figs. 1–4). This leads to depolarization within the telescope beam, observed as a ‘depolarization valley’ parallel to the emitting ridge. This was first

observed in NGC 1097 by Beck et al. (1999). Our new data show that the valley persists when observed with higher angular resolution. Its structure is similar at both wavelengths so that it cannot be produced by Faraday depolarization. The average distance between the depolarization valley and the ridge in polarized intensity is $10''$ (≈ 800 pc) in NGC 1097 and $11''$ (≈ 1.0 kpc) in NGC 1365.

The observed width of the depolarization valley, defined as the distance between points where the polarized intensity drops to half the value outside the valley, is about $4''$ (≈ 300 pc) in NGC 1097 (Fig. 1) and about $6''$ (≈ 500 pc) in NGC 1365. This is the scale at which the regular magnetic field is deflected. Note that a value of the width smaller than the resolution is reliable because the deflection valley appears only in the map of polarized intensity (which is not a directly observed quantity). In the maps of the observed quantities, the Stokes parameters Q and U , the valley is represented by a smooth variation with a sign reversal at the location of the depolarization valley. The width of the valley depends on the gradients in Q and U . Beam smearing decreases these gradients, so that the intrinsic width is smaller than that given above.

According to our $\lambda 6.2$ cm data of NGC 1097 with high signal-to-noise ratio (right-hand panel of Fig. 2), the field orientation turns smoothly within a distance of about $20''$ (1.6 kpc) upstream of the ridge. Both depolarization and field bending are discussed in Sect. 8.3. In NGC 1365 the turning of the field lines is smoother and the depolarization valley is broader than in NGC 1097.

Figure 10 shows the intrinsic magnetic field orientations in both galaxies, derived from the B -vectors at $\lambda 3.5$ cm and $\lambda 6.2$ cm, corrected for Faraday rotation (see Sect. 3.4) and deprojected into the galaxies’ planes.

The intrinsic magnetic field in the southern ridge of NGC 1097 follows the dust lane orientation (left-hand panel of Fig. 10). The orientation of the field and that of the dust lane generally agree in the northern bar of NGC 1097 as well, but both are less pronounced than in the south. As the northern half appears distorted in all

spectral ranges, we suspect gravitational distortion by the companion galaxy NGC 1097A. In NGC 1365 the field in the eastern ridge is along the dust lane, but the resolution is insufficient to trace details.

In the southern bar of NGC 1097 (at $35''$ – $50''$ or 3–4 kpc distance from the centre) the intrinsic pitch angle of the magnetic field obtained from the polarized emission (i.e., the angle between the field orientation and circumference) jumps from about 15° (almost azimuthal) in the upstream region (west of the southern ridge) to about 75° (almost radial) in the southern ridge (see the left-hand panel of Fig. 10), which yields a deflection angle of about 60° . The deflection angle decreases to about 40° at around $60''$ radius; this decrease is accompanied by a reduction in the contrast in magnetic field strength (see Table 3). In NGC 1365 (see the right-hand panel of Fig. 10), the deflection angle is about 70° in the inner eastern bar.

The orientations of the field lines do not everywhere follow those of the gas streamlines (in the corotating frame) of the hydrodynamic models of Athanassoula (1992b) and the models for NGC 1365 by Lindblad et al. (1996). It is instructive to compare the right-hand panel of Fig. 10 and Fig. 26b of Lindblad et al. (1996), where it appears that the alignment is reasonably tight in the northern part of the galaxy, but not in the southern part. This is discussed in detail in Sect. 7.2.

The intrinsic field orientation upstream of the southern bar of NGC 1097 (left-hand panel in Fig. 10) follows the small, feather-like dust filaments located upstream of the main dust lanes as seen in the optical image (Fig. 2, around RA, DEC(J2000) = 02 46 21, -30 16 25). The reason for this alignment and the origin of the filaments are unknown.

The structure of the incoherent and coherent magnetic fields is further discussed in Sects. 8.2.1 and 8.3.

3.4. Faraday rotation and depolarization in the bar region

The polarization angles at $\lambda 3.5$ cm and $\lambda 6.2$ cm of NGC 1097 and NGC 1365 with $10''$ and $25''$ resolution, respectively, were used to derive maps of the Faraday rotation measure RM (measured in rad m^{-2}) shown in Fig. 11. The ambiguity in RM due to the $\pm\pi$ uncertainty in polarization angle is $\pm 1232 \text{ rad m}^{-2}$. The Faraday rotation measure RM is proportional to the product of thermal electron density n_e (in cm^{-3}) and the line-of-sight component B_{\parallel} of the regular magnetic field (in μG), integrated over the path length L (in pc): $\text{RM} = 0.81 \int n_e B_{\parallel} dL$.

RM in NGC 1097 (top left panel of Fig. 11) is generally positive on the western and negative on the eastern side of the inner southern ridge, with a jump at the position of the depolarization valley, where the orientation of the field B_{\perp} in the sky plane also turns rapidly (see Sect. 3.3). This discontinuity in the magnetic field is weaker in the middle ridge and vanishes in the outer ridge. However, the

errors in RM increase with increasing distance from the centre due to the decreasing polarized intensities.

Figure 12 shows the azimuthal variation of RM in two rings in the plane of NGC 1097. In the inner ring (left-hand panel), west of the southern ridge (at 190° azimuthal angle), RM *reverses its sign* and jumps by about 500 rad m^{-2} , which corresponds to a change of the polarization angle by about 110° at $\lambda 6.2$ cm and by about 35° at $\lambda 3.5$ cm. At larger radii (right-hand panel of Fig. 12), the RM jump decreases to about 200 rad m^{-2} . In the outer bar ($45''$ – $75''$ radius, not shown), RM does not jump, but changes smoothly by about 300 rad m^{-2} within a range of 50° in azimuthal angle.

Negative RM in the southern bar means that the line-of-sight component of the magnetic field points away from us. Knowing that the position angle of the major axis of the projected plane of NGC 1097 is -45° with the southwestern side being nearer to us, the radial component of the magnetic field in the ridge points *inwards* (i.e. towards the galaxy's centre).

In the northern ridge of NGC 1097, signal-to-noise ratios are low, so that RM can be determined only with low accuracy. RM values of $+100 \text{ rad m}^{-2}$ around 330° azimuth (Fig. 12) show that the regular magnetic field along the ridge also points towards the centre and has a similar strength to that in the southern ridge.

RM in NGC 1365 (bottom left panel of Fig. 11) is measured only in the central region (Sect. 5.2) and a few patches between the spiral arms. The polarized emission in NGC 1365 is generally weaker than that in NGC 1097.

Faraday depolarization DP (defined as the ratio of the degrees of polarization at $\lambda 6.2$ cm and $\lambda 3.5$ cm) is shown in the right-hand column of Fig. 11. The amount of depolarization is small ($\text{DP} \simeq 1$) in the outer ridge and upstream regions of NGC 1097, but increases towards the centre ($\text{DP} \simeq 0.5$) where the turbulent field strength is presumably larger. Depolarization in NGC 1365 is stronger ($\text{DP} = 0.3$ – 0.6 in the ridges and in the spiral arms) than in NGC 1097, possibly due to larger thermal plasma density, but the data are of limited quality as polarized intensity is low at $\lambda 3.5$ cm.

3.5. Field structure in the outer regions and spiral arms of NGC 1097

The optical image of NGC 1097 (Fig. 1) shows an elliptical structure of about $3'.5 \times 2'$ in size, connecting the ends of the bar. The ellipse is also the outer edge of the disc-like diffuse optical emission. This ellipse can reflect one family of orbits in a typical bar potential (see, e.g., Fig. 12 in Athanassoula 1992a). Highly polarized radio emission emerges from along most of this feature (Fig. 3), with B -vectors mostly tangent to it. This indicates that the regular magnetic field is aligned with the gas flow in this region.

The spiral arms are clearly visible in radio continuum, at least the parts which are near to the galaxy's centre.

The orientation of the B -vectors at $\lambda 6.2$ cm is along the inner northern spiral arm, but almost perpendicular to the outer arm in the south-west (Fig. 3). Strong Faraday rotation seems improbable at such large radii, hence the field must be distorted, presumably together with the gas flow.

3.6. The magnetic field strength in the bar regions

We computed the strengths of the total B_I and regular + anisotropic random fields B_P in the radio ridges of NGC 1097 and NGC 1365 from the total synchrotron intensity I_s and the degree of polarization p of the synchrotron emission, using the maps at $\lambda 6.2$ cm at $10''$ and $15''$ resolution, respectively. (Although at $\lambda 6.2$ cm Faraday depolarization may be significant in some regions, we preferred to use this wavelength because of the higher signal-to-noise ratios than at $\lambda 3.5$ cm.) I_s followed from the total intensity by subtracting the thermal fraction estimated from the observed spectral index α between $\lambda 3.5$ cm and $\lambda 6.2$ cm (Table 3).

We further assumed equipartition between the energy of the total magnetic field and that of the cosmic rays (protons + electrons), with a number density ratio K of cosmic ray protons to electrons of 100 in the relevant (GeV) energy range, a path length through the synchrotron-emitting medium of $L = 500$ pc (similar to the intrinsic width of the ridges of NGC 1097, see Sect. 3.2), and a synchrotron spectral index of $\alpha_s = -1$. We applied the revised equipartition formula of Beck & Krause (2005). (For field strengths beyond $10 \mu\text{G}$ and for $\alpha_s \leq -1$ the revised formula gives smaller field strengths than the classical estimate.) The results for B_I and B_P are given in Table 3. These estimates scale with $(K/L)^{1/(3-\alpha_s)}$, so that even an uncertainty in K or L of 40% would cause an error in B of only 10% (for $\alpha_s = -1$).

The ridges in total and polarized intensity are produced by an increase in B_I and B_P due to compression and shear. The strong anisotropy in the random magnetic field caused by compression is the main contributor to the increased intensity (Sects. 8.1 and 8.2.1).

The observed RM can be used to estimate the strength of the component \overline{B}_{\parallel} of the regular field \overline{B} along the line of sight if the thermal electron density and the path length are known. In principle the thermal electron density of the Faraday rotating layer can be derived from an estimate of the emission measure of the thermal radio emission. The resulting estimates for \overline{B}_{\parallel} depend on the uncertain quantities EM, L and the volume filling factor η of thermal electrons to the power $-1/2$, and are thus more sensitive to the assumed parameters than in the equipartition estimate. Bearing this in mind, for an estimated EM of $100 \text{ cm}^{-6} \text{ pc}$ in the southern ridge of NGC 1097 (where the thermal fraction f_{th} is about 0.05, see Table 3), using Eq. (1) in Ehle & Beck (1993), assuming that 20% of this emission measure is due to diffuse gas ($\eta = 0.2$, as in normal spiral galaxies, e.g. Greenawalt et

al. 1998), and taking a path length $L = 500 \text{ pc}$, we obtain $\overline{n}_e = (\text{EM}\eta/L)^{1/2} \simeq 0.2 \text{ cm}^{-3}$. For an RM of 100 rad m^{-2} observed in the southern ridge, this gives a strength of the regular magnetic field component along the line of sight of $\overline{B}_{\parallel} = \text{RM}/(0.81\overline{n}_e L) \simeq 1 \mu\text{G}$.

To compute the full regular magnetic field strength \overline{B} , the angle ϕ_1 between the field and the sky plane has to be known. If the regular field is directed along the ridge, the position angle of the field in the sky plane with respect to the galaxy's major axis is $\phi_2 \simeq 20^\circ$. However, the left-hand panel of Fig. 13 indicates that the regular field may have a position angle of about 45° in the galaxy plane, or $\phi_2 \simeq 35^\circ$ in the sky plane. The angle ϕ_1 between the regular field and the sky plane follows from $\tan \phi_1 = \tan \phi_2 \sin i$ where $i = 45^\circ$ is the galaxy's inclination, and the regular field strength follows from $\overline{B} = \overline{B}_{\parallel}/\sin \phi_1$. For the range of probable ϕ_1 values, we derive $\overline{B} \approx 2 - 4 \mu\text{G}$. This is significantly lower than the value obtained from polarized intensity, $B_P \simeq 12 \mu\text{G}$, strongly suggesting that a substantial fraction of the polarized emission is due to anisotropic random magnetic fields (Sect. 8.2.1).

3.7. Magnetic field strengths in the spiral arms, disc, and envelope

Substantial radio emission has been detected in the northern spiral arm of NGC 1097, which emerges from the northern end of the bar (around RA, DEC(J2000) = 02 46 25, -30 14 15, see Figs. 1 and 3). The magnetic field orientation suggested by the polarization angles is along the arm. The mean degree of polarization is low at $\lambda 3.5$ cm and $\lambda 6.2$ cm ($p \leq 5\%$). The mean equipartition magnetic field strengths obtained from the total synchrotron emission (after subtraction of 30% thermal emission) and polarized radio emission in the northern arm are $B_I \simeq 18 \mu\text{G}$ and $B_P \simeq 6 \mu\text{G}$, respectively.

Bright radio emission outside of the bar of NGC 1097 is also detected in the elongated region emerging from the end of the southern bar towards the west (around RA, DEC(J2000) = 02 46 20, -30 17 50, see Fig. 2). Here the degree of polarization is quite high ($p \simeq 10\%$). The equipartition strengths of magnetic fields obtained from the total synchrotron and polarized radio emissions are $B_I \simeq 22 \mu\text{G}$ and $B_P \simeq 10 \mu\text{G}$, respectively. This feature appears to be a part of the ring-like structure discussed in Sect. 3.5.

The distribution of RM in NGC 1097 does not show any systematic variation in the region of the spiral arms beyond the bar. However, the RM errors are large due to the weak polarized emission.

The spiral arms of NGC 1365 are brighter than those in NGC 1097 both in optical light and in radio continuum (Fig. 4), while the degree of radio polarization is similarly low ($p \leq 5\%$) in both galaxies. The mean equipartition strengths of magnetic fields obtained from the total synchrotron and polarized radio intensities are about

$22\,\mu\text{G}$ and $3\,\mu\text{G}$, respectively, for the north-western arm of NGC 1365, and about $18\,\mu\text{G}$ and $5\,\mu\text{G}$ for the south-eastern arm.

In the low-resolution images, both galaxies exhibit an envelope of diffuse radio emission (Figs. 3 and 5) where the degree of polarization is high, typically 25% at $\lambda 6.2\,\text{cm}$. Assuming that the emission emerges from an extended disc with a path length of 1 kpc, negligible thermal emission and a synchrotron spectral index of $\alpha_s = -1$, we obtain $B_I \simeq 13\,\mu\text{G}$ and $B_P \simeq 7\,\mu\text{G}$ for NGC 1097, and $B_I \simeq 9\,\mu\text{G}$ and $B_P \simeq 5\,\mu\text{G}$ for NGC 1365. If, however, the diffuse emission emerges from a *halo* with a path length of 10 kpc, the fields are weaker by a factor of about 1.8.

4. The global magnetic structures

The *large-scale structure and direction of the regular magnetic field* in a galaxy can be recovered from polarization position angles at more than one frequency. We have applied a method that seeks to find statistically good fits to the polarization angles of synchrotron emission, of a superposition of azimuthal magnetic field modes $\exp(im\phi)$ with integer m , where ϕ is the azimuthal angle in the galaxy's plane. We have used $\lambda\lambda 3.5, 6.2\,\text{cm}$ polarization angles of NGC 1097 ($10''$ resolution) and NGC 1365 ($15''$ resolution), averaged in sectors with opening angles in azimuth of 10° and 20° , respectively. The nuclear regions, inside the innermost rings in Fig. 13, suffer from strong Faraday depolarization (see the right-hand panel of Fig. 11) and hence represent a different problem for modelling that should be addressed elsewhere.

A three-dimensional model of regular magnetic field is fitted to the observations of polarization angles at both wavelengths simultaneously. The polarization angle affected by Faraday rotation is given by $\psi = \psi_0 + \text{RM}\lambda^2$, where the intrinsic angle ψ_0 depends on both the regular magnetic field and the anisotropic random field (both in the sky plane), whereas the second term is only sensitive to the regular magnetic field. The vector of the regular magnetic field is specified in terms of a Fourier expansion in azimuth, and ψ_0 and RM are derived consistently with each other. Then the coefficients of the Fourier series are fitted to the observed angles using nonlinear least squares techniques, and the quality of the fits is verified using statistical criteria. The method, and its application to data from two spiral galaxies, is described in more detail in Berkhuijsen et al. (1997) and Fletcher et al. (2004). The fitted parameters of the regular magnetic fields in the two galaxies are given in Appendix B. The fit parameters given there can be used to reconstruct the global magnetic structures in the galaxies. The resulting regular magnetic field structures of the two barred galaxies are shown in Fig. 13. We applied this method to NGC 1097 also in Moss et al. (2001), but there used data with lower resolution. With our new polarization data we can increase the number of sectors, and hence the spatial sensitivity of the model, by a factor of 2.

As discussed in Sect. 3.6, a significant part of the polarized emission can be due to a random anisotropic magnetic field (which does not contribute to Faraday rotation). Therefore, our fits can be a poor representation of the observed polarization angles where the anisotropic random field is strong and misaligned with the regular magnetic field. The regions where the anisotropy of the random field is strong are the radio ridges. The anisotropic and regular fields are affected by compression in a different way (Sect. 8.2.3). However, we reasonably expect that the anisotropy produced by compression and shear will be roughly aligned with the regular magnetic field, as indicated by comparing Figs. 13 and 10.

4.1. NGC 1097

We were unable to achieve a statistically good fit to the data for the inner ring ($15'' < r < 30''$, $1.25 < r < 2.5\,\text{kpc}$) of NGC 1097 using combinations of up to three modes selected from $m = 0, 1, 2, 3, 4$ for the horizontal magnetic field, combined with either a uniform or a 2π -periodic vertical magnetic field. The reason for this is the sharp discontinuity and sign change in the Faraday rotation measures at the southern end of the bar major axis, shown in Fig. 12 and discussed in Sect. 3.4. However, a statistically good regular magnetic field model can be readily obtained by treating separately the two halves of the ring on either side of the bar axis. Then each half can be satisfactorily described by the combination of modes $m = 0, 2$. To the north-east of the major axis (azimuth 20° to 190° measured from the northern end of the major axis), the $m = 2$ mode is twice as strong as the $m = 0$ mode. In the other half of the galaxy, the two modes have similar amplitudes.

The motivation for splitting this ring into two halves is that strong shear in the velocity field in the bar results in an abrupt change in sign of the radial component of the magnetic field. This type of sudden change, giving rise to the discontinuity and sign change in RM, cannot be well described by a superposition of a small number of azimuthal modes.

The regular magnetic field pattern required to model the $\lambda\lambda 3.5, 6.2\,\text{cm}$ polarization angles – and hence the RM discontinuity in Fig. 12 – between $1.25 < r < 2.5\,\text{kpc}$ in NGC 1097 is shown in Fig. 13 (left-hand panel). At the southern end of the bar, slightly upstream of the bar axis, the radial and azimuthal components of the coherent regular magnetic field change sign. At the same location the pitch angle of the field abruptly increases from $p_A = 27^\circ$ to $p_A = 41^\circ$. (Note that the change in p_A is less than the deflection angle discussed in Sect. 3.3 due to averaging of the observations in sectors; we lose spatial resolution using the model but gain the *direction* of the regular field.) This sharp change in the regular field may be a sign of strong shear and compression, and this possibility is discussed in Sect. 8.3. Three more reversals in the regular magnetic field are also apparent in this ring. Two of these

are smoother transitions from positive to negative RM and do not produce RM discontinuities (Fig. 12). At the north end of the bar there is a stronger and sharper reversal that resembles that in the south. However, the weak regular field in the north-west of the bar (Fig. 1) means the global pattern is less apparent here.

The second ring ($30'' < r < 45''$, $2.5 < r < 3.75$ kpc) was also modelled by splitting the data into two halves, on either side of the bar axis. In this case though, no reversals in the regular magnetic field are required (see the left-hand panel of Fig. 13). The variation in RM shown in Fig. 12 (right-hand panel) is not as dramatic as in the inner ring and the observed sign reversals of RM are consistent with projection effects due to the galaxy's inclination. Our fits for the whole ring are consistent with those for the two halves reported here. The regular field in this ring is nearly azimuthal, especially in the half of the galaxy south east of the major axis. In both halves of the galaxy the modelled field consists of a strong axisymmetric component and a weaker higher azimuthal mode. Neither the radial nor the azimuthal components of the coherent regular field change sign in the model. Although the observed RM seem to change sign at $\phi \simeq 190^\circ$ (right-hand panel of Fig. 12), the error bars are large, so that the model curve is a statistically good fit. The change in magnetic field pitch angle at the southern end of the bar major axis is in the same sense as for the inner ring. The change in the pitch angle from the purely azimuthal upstream field ($p_A \simeq 0^\circ$) to the deflected field downstream of the bar is $\simeq 40^\circ$.

For the third ring ($45'' < r < 60''$, $3.75 < r < 5$ kpc), we did not split the magnetic field into two halves; there is little sign of an RM discontinuity in this ring. Again the regular magnetic field is nearly azimuthal in the southern half of the galaxy and is deflected after passing through the dust lane. The fitted regular field in this ring comprises a strong $m = 0$ mode and two higher modes ($m = 1, 2$) with amplitudes which are about half as large.

4.2. NGC 1365

Polarized emission in NGC 1365 can be traced to larger radii than in NGC 1097, so that more rings can be included in our analysis. The polarization angles in the rings shown in Fig. 13 (right-hand panel) were fitted with a combination of $m = 0, 1$ and 2 modes, except for the third ring from the centre where only modes $m = 0, 2$ were required. The fit parameters are given in Table B.2. There is a tendency for p_A to become larger (a less azimuthal, more radial field) approaching the bar from the upstream direction, although this is not the case in all rings. The amount of deflection in the field orientation is weaker than in NGC 1097.

A reversal is detected in the regular magnetic field direction in the north-west quadrant (upper right) of the second ring from the centre. This is not seen in the RM map (bottom left panel of Fig. 11), but only becomes ap-

parent when the data is averaged into sectors and modelled. This reversal is similar to that seen in the ridge of NGC 1097. Since the weaker signal from NGC 1365 means we had to use only sectors with an opening angle of 20° compared to 10° in NGC 1097, it is possible that further reversals will be revealed with more sensitive polarization observations.

5. The central regions

5.1. NGC 1097

Both galaxies studied in this paper host a central starburst region. The circumnuclear ring of NGC 1097 is a prototype example of mass inflow and starburst ignition in a bar potential and has been studied in various spectral ranges (Gerin et al. 1988, Barth et al. 1995, Quillen et al. 1995, Pérez-Olea & Colina 1996, Kohno et al. 2003). In high-resolution infrared images, the ring is resolved into a complex network of filamentary spiral features (Prieto et al. 2005).

The radio continuum ring in NGC 1097 was first studied in detail by Hummel et al. (1987). It appears as an almost perfect ring with an average radius of $9''0$ (740 pc) ($9''5$ in north-south and $8''5$ in east-west directions). Although it seems that the ring lies in the sky plane, the line-of-sight gas velocity is as large as 230 km s^{-1} at position angle -45° (Gerin et al. 1988), indicative of the ring actually lying in the galaxy's plane and being intrinsically elongated along the line of sight. The radio spectrum of the ring is nonthermal (see below) so it must contain strong magnetic fields. Beck et al. (1999) detected polarized emission from this ring. Our new data have much higher resolution and also allow us to measure Faraday effects.

The radio map of NGC 1097 at our highest resolution, shown in the top left panel of Fig. 14, exhibits several prominent knots in total intensity, mostly coincident with optically prominent star-forming regions. The three brightest knots are separated by almost precisely 120° in azimuthal angle (being located at position angles 15° , 135° and 255° , measured anticlockwise from the north). No similar periodicity is seen in polarized intensity. Elmegreen (1994) proposed that the gravitational instability can be responsible for the fragmentation of inner rings into clouds.

The spectrum is significantly flatter in the knots of the circumnuclear ring ($\alpha = -0.65 \pm 0.02$) than between them ($\alpha = -0.72 \pm 0.02$) (see Fig. 9) which can be due to a higher thermal fraction, as suggested by Hummel et al. (1987). Assuming the same synchrotron spectral index of $\alpha_s = -1$ as in the ridges (see Sect. 3.2), the thermal fraction f_{th} at $\lambda 3.5$ cm is 45% in the knots and 35% in between. If the observed spectral index is smaller than α_s , the thermal fraction cannot be determined, and then we assume that it is negligible. However, the synchrotron spectral index α_s in the knots could be larger than -1 , e.g. due to a contribution of radio emission from individ-

ual young supernova remnants which are expected to have an average spectral index of $\alpha_s \simeq -0.6$. Furthermore, if bremsstrahlung loss of the cosmic-ray electrons dominates over synchrotron loss, the synchrotron spectral index is the same as the intrinsic one ($\alpha_0 = -0.5$ for strong shocks). In this case the observed spectral indices are similar to the synchrotron spectral index so that the thermal fractions are small. An independent estimate of the thermal emission from the optical H α line is impossible as the quality of the existing data is insufficient.

The equipartition strength of the total magnetic field in the knots of NGC 1097 is about $60 \mu\text{G}$ (assuming a synchrotron spectral index of $\alpha_s = -1.0$ and a path length of 500 pc), applying the revised equipartition formula by Beck & Krause (2005). The average total field strength in the central ring is about $55 \mu\text{G}$. The field strength is somewhat larger than that given by Beck et al. (1999) because here we assumed a steeper synchrotron spectrum and a smaller path length. The degree of polarization in the knots is low (1–3%), yielding a regular + anisotropic random field of $B_P \simeq 10 \mu\text{G}$ (Table 4). Alternatively, for $\alpha_s = -0.7$ and generally negligible thermal emission, the total field strength in the knots increases to about $70 \mu\text{G}$, while B_P decreases to $4\text{--}8 \mu\text{G}$.

At the positions where the radio ridges and dust lanes enter the central ring of NGC 1097, the degree of polarization is much higher (note maxima in north-east and south-west in Fig. 14, bottom row panels) which yields $B_P \simeq 20 \mu\text{G}$ (Table 4).

The regular (or anisotropic random) magnetic field in the central region of NGC 1097 is of a spiral shape and extends well inside the ring (see the top right panel of Fig. 14). The equipartition strength of the magnetic field obtained from polarized emission, B_P , is about $15 \mu\text{G}$ inside of the ring (north of the centre) (Table 4).

Faraday rotation measures are generally small in the ring of NGC 1097 (top left panel of Fig. 11). The RM jump in the southern ridge (see Fig. 12) continues into the ring. With such small RM values, it is impossible to separate the coherent and anisotropic random field components as attempted in the southern bar region (Sect. 3.6). We suspect that, in contrast to the ridges, most of the polarized emission from the ring originates in a coherent magnetic field, as the conditions for dynamo action are perfect: high star-formation rate and strong differential rotation velocity of order 330 km s^{-1} (Gerin et al. 1988, Kohno et al. 2003). Note that the average pitch angle of the spiral field, corrected for Faraday rotation, is about $39^\circ \pm 3^\circ$, which is larger than in the discs of typical spiral galaxies. This fact also supports strong dynamo action. However, small RM and strong Faraday depolarization (see below) in our present data prevent a search for global modes in the structure of the coherent regular field. New observations with higher sensitivity at shorter wavelengths (where Faraday depolarization is weaker) are required.

Prieto et al. (2005) interpret the spiral magnetic field in the central region of NGC 1097 as indication of a flow of warm gas far away from the galaxy's plane, crossing the

circumnuclear ring. Detailed measurements of Faraday rotation are necessary to clarify the geometry of the magnetic field structure.

Faraday depolarization between $\lambda 3.5 \text{ cm}$ and $\lambda 6.2 \text{ cm}$ is strong in the ring of NGC 1097 (Fig. 11, and compare Fig. 14, bottom row panels), evidently a result of strong turbulent fields and high thermal electron density. Only the western tangential point has the same polarized intensity at both wavelengths. The ridge emerging on the western (near) side lies in front of the ring where it cannot be depolarized by the medium in the ring. The hot thermal gas of the halo detected in X-rays is too thin to cause significant Faraday depolarization at $\lambda 6.2 \text{ cm}$ (Sect. 6).

The nucleus of NGC 1097 has a flat spectrum with a spectral index of $\alpha \simeq -0.05$, typical for active nuclei. An investigation of its properties is beyond the scope of this paper.

5.2. NGC 1365

NGC 1365 has a central starburst region which is even brighter in radio continuum than the central ring in NGC 1097, and hence the total equipartition fields are even stronger. The peak value of about $63 \mu\text{G}$ in the inner part of the massive dust lane located south of the centre is one of the largest field strengths found in any normal or barred spiral galaxy so far. Stronger fields were observed only in the circumnuclear rings of the southern barred galaxies NGC 1672 and NGC 7552 (Beck et al. 2005). The degree of polarization in the inner dust lane (Table 4) is lower than that in the ring of NGC 1097 (Table 3). In the outer part of the same dust lane, south-west of the centre, and in the outer part of the eastern dust lane, the degrees of polarization increase significantly. The pitch angle of the regular field in the ring (radial range $7''.5\text{--}22''.5$, or $0.7\text{--}2.0 \text{ kpc}$) varies strongly between 0 and -70° .

RM shows a jump in the central region of NGC 1365, south of the nucleus (bottom left panel of Fig. 11). A similarity to the field reversal in the ridges of NGC 1097 and NGC 1365 is possible, but needs investigation with future data at higher resolution.

6. The X-ray halo of NGC 1097

In order to determine the strength of regular fields from Faraday rotation measures, independent information is needed about electron density (Sect. 3.6), e.g. from thermal radio or H α emission which is significant from gas at a temperature at a few 1000 K . Hot gas, as observed with X-rays, may also contribute to Faraday effects.

The soft X-ray emission from NGC 1097 observed with *ROSAT* (Fig. 16) peaks at the galactic nucleus, which could be expected as NGC 1097 is known to harbour an active Seyfert nucleus. In addition to the nuclear emission (which is smoothed out to a galactocentric radius of about $1'$, corresponding to the point spread function of the PSPC at low energies), the soft X-ray emission has contours elongated along the spiral arms and the bar, and was

Table 4. Properties of the central parts of NGC 1097 ($r < 1$ kpc) and NGC 1365 ($r < 2$ kpc) from the $\lambda 3.5$ cm data. The locations of the regions are described in the text. The thermal fractions were determined with the assumption of a synchrotron spectral index of $\alpha_s = -1.0$.

	Thermal fraction	Synchrotron polarization [%]	B_I [μ G]	B_P [μ G]
NGC 1097				
Bright knots	0.45	2	60	10
Tangential point (W)	0.35	15	56	21
Tangential point (E)	< 0.05	37	34	21
Inside the ring (N)	0.45	17	40	15
NGC 1365				
Inner dust lane (S)	0.35	0.5	63	6
Outer dust lane (SW)	< 0.05	4	38	9
Outer dust lane (E)	< 0.05	22	21	12

even detected outside the bar. This indicates the presence of extended hot gas in a disc and/or in a halo.

The soft X-ray spur in the north-west points towards the companion galaxy NGC 1097A (Ondrechen et al. 1989) and might be a signature of ongoing tidal interaction between the two galaxies.

Our successful spectral fit to the dominating X-ray emission (background-corrected) from the central region of NGC 1097 within a galactocentric radius of $1'$ used a combined emission model including a power law component (to describe the nucleus and unresolved point-like sources) and a Raymond–Smith plasma with ‘cosmic’ metal abundances (Raymond & Smith 1977), both affected by Galactic foreground absorption (with hydrogen column density of $1.87 \times 10^{20} \text{ cm}^{-2}$). With the fitted temperature of $9.6 \times 10^6 \text{ K}$ and photon index s of 1.3 (where the X-ray flux density is proportional to E^{-s}), the luminosity of the inner part of NGC 1097 in the total ROSAT energy band (0.1–2.4 keV) was found to be $11.8 \times 10^{40} \text{ erg s}^{-1}$, with about 84% of it originating from the power law component.

Unfortunately, the X-ray count rate statistics of the extended component outside a radius of $1'$ (where we expect that the emission is no longer affected by the Seyfert nucleus) were too poor to allow a separate fit of this emission component. Higher sensitivity X-ray observations of NGC 1097, e.g., with XMM-Newton, are needed to further constrain this unresolved emission. Assuming a Raymond–Smith plasma with $T = 2.3 \times 10^6 \text{ K}$ (which seems to be typical of the X-ray emitting hot gas in spiral galaxies) and correcting for the background and the Galactic foreground absorption, the count rate of $2.86 \times 10^{-2} \text{ counts s}^{-1}$ in the outer area corresponds to an X-ray luminosity of $1.65 \times 10^{40} \text{ erg s}^{-1}$ in the energy range 0.1–2.4 keV.

The plasma density n_e of the extended component can be calculated under the assumption of radiative cooling and ionization equilibrium (Nulsen et al. 1984), where the luminosity in soft X-rays is given by $L_X = 1.11 \times \Lambda(T) n_e^2 V \eta$, with Λ the cooling rate, V the emitting volume and η the filling factor of the emitting gas. For our assumed gas temperature, Raymond et al. (1976) give a cooling coefficient $\Lambda(T)$ of about $10^{-22} \text{ erg cm}^3 \text{ s}^{-1}$. To ad-

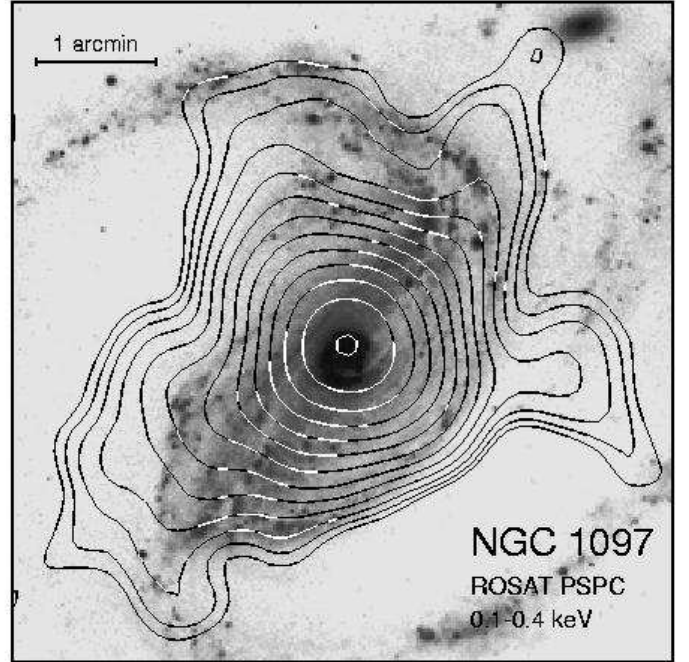


Fig. 16. Soft-band (0.1–0.4 keV) X-ray emission from NGC 1097, observed with the ROSAT PSPC detector. Contour levels are $2^{n/2} \times 3 \cdot 10^{-4} \text{ counts s}^{-1} \text{ arcmin}^{-2}$ ($n = 1, 2, \dots$) above the background of $12 \cdot 10^{-4} \text{ counts s}^{-1} \text{ arcmin}^{-2}$. The background optical image was kindly provided by Halton Arp.

dress the possibility that the emitting plasma is located in the disc of NGC 1097 we assumed a cylindrical volume (inner radius $1'$, outer radius $4'$ and a disc path length of 1 kpc) to obtain an electron volume density of $n_e \simeq 3.4 \times 10^{-3} \eta^{-1/2} \text{ cm}^{-3}$. If the thermal energy density of the hot gas is equal to that of the magnetic field, as is the case in other diffuse phases of the ISM, the total field strength should be $5.2 \mu\text{G} \times \eta^{-1/4}$. The total field strength in the interarm space between the bar and the northern spiral arm is estimated from the total radio emission as about $13 \mu\text{G}$ (assuming equipartition with the cosmic rays and an average path length of 1 kpc). Thus, either the fill-

ing factor of the hot gas is as small as 3%, or the magnetic field energy density is larger than the thermal energy density, or the magnetic field obtained from radio emission is overestimated.

Note, however, the asymmetry of the extended soft X-ray emission, which is stronger and falls off more slowly on the north-eastern (far) side of the galaxy than on the south-western (near) side (Fig. 16). This may indicate that a large fraction of the extended X-ray emission emerges from a quasi-spherical halo of hot gas in front of an absorbing (cool) gas disc. Assuming in this case a halo radius of 10 kpc (and excluding again the inner radius out to $1'$), we obtain an electron volume density of $n_e \simeq 2.3 \times 10^{-3} \eta^{-1/2} \text{ cm}^{-3}$. A total magnetic field of $5 \mu\text{G} \times \eta^{-1/4}$ would be in equipartition with thermal energy. If the diffuse radio emission around NGC 1097 emerges from a halo, the total field strength is about $7 \mu\text{G}$ (Sect. 3.7), which agrees well with the above estimate from the soft X-ray emission for a filling factor $\eta \simeq 0.3$.

As the degree of polarization is about 25% (see Sect. 3.7), about half of the total field in the halo (or disc) is coherent (if the anisotropic random field is negligible). The expected Faraday rotation for a coherence length of 1 kpc is about $5 \times \eta^{-3/4} \text{ rad m}^{-2}$, which is much too small to explain the observed Faraday rotation. We conclude that the hot halo gas around NGC 1097 does not contribute to Faraday effects.

7. Models of gas flow and magnetic field in the bar region

In this and the following sections, we interpret the radio maps in terms of magnetic field models and discuss their compatibility with gas-dynamical models of barred galaxies.

The most important assumption of our interpretation is the existence of a shock. Note that shear shocks in bars behave differently from classical shocks, and the compression region may extend deeply into the downstream region (Syer & Narayan 1993). No 3-D models of shear shocks including magnetic fields are available yet.

The best observational tool to identify the location of the gas shock is the velocity field of the cold, dense gas. In NGC 1097 H I line emission from the bar is very weak so that the velocity field is known only in the outer spiral arms (Ondrechen et al. 1989). CO line emission from the bar is also weak, and the resolution is insufficient to resolve the shock front (Crosthwaite 2001). Velocity fields in the bar region were published for a few other galaxies. Steep velocity gradients occur across the dust lanes in NGC 1365 (Jörsäter & van Moorsel 1995, Lindblad et al. 1996) and in NGC 1530 (Reynaud & Downes 1998) which indicate that the deflection and compression regions indeed coincide. Sensitive observations of the velocity field of NGC 1097 and NGC 1365 in the H I and CO lines are required to localize the shock fronts and to measure their compression ratio and their rate of deflection in the flow

direction. Hence there is sufficient evidence for shocks in both galaxies of our study.

Perhaps the most notable features of gas flow in barred galaxies are dust lanes extended along the leading edge of the bar, which are identified with large-scale shocks in the interstellar gas (Athanasoula 1992b). Strong gas compression and velocity shear are expected to occur in the dust lanes. Therefore, it is not surprising that they host enhanced magnetic fields and appear as bright radio ridges in the radio maps discussed in Sect. 3.2.

Our observations have revealed several unexpected features of both regular and random magnetic fields which are similar in both galaxies and may be characteristic of barred galaxies in general. The regular magnetic field does not seem to be perfectly aligned with gas streamlines in the reference frame corotating with the bar. In both galaxies, the regular magnetic field upstream of the bar is approximately perpendicular to the dust lanes. The field then apparently begins to turn and becomes parallel to the dust lanes at their position (see Sect. 3.3, and Figs. 2 and 5). Hydrodynamic models of the gas flow in generic barred galaxies (e.g. Athanasoula 1992b) have streamlines that behave quite differently, with an acute change in the direction of the flow at the leading side of the bar. Two possible explanations for this effect are discussed in Sect. 7.1 and 7.2.

In Sect. 8.1 we show that the enhancement in total radio emission observed from the radio ridges is compatible with compression and shearing of a random magnetic field in the shock at the dust lanes. It is striking, however, that the observed enhancement in polarized intensity indicates that the regular magnetic field avoids any significant amplification by compression and shear in the shock. This behaviour is surprising indeed as the effects of compression and shearing are clearly seen in total radio emission, as well as in the gas distribution and kinematics. In Sect. 8.2.3 we attribute this peculiar behaviour of the regular magnetic field to the effects of conversion of atomic gas to molecular form in the shock (i.e., the dust lane).

7.1. The effect of inclination and beam smoothing

The apparent offset of the depolarized strip from the dust lane and the early onset of the magnetic field deflection could be a geometrical effect due to the inclination of the galaxy's disc and the integration of the emission along the line of sight through the disc. Here we demonstrate the potential consequences of these effects using synthetic maps produced from a simple model of the galaxy in which the magnetic field sharply changes its direction by 90° in the bar.

We prescribe a magnetic field in the plane of the model galaxy in cylindrical coordinates (r, ϕ, z) , with ϕ measured in the galaxy's plane from the northern and western end of the bar major axis to model NGC 1097 and NGC 1365, respectively, and the positive z -direction being

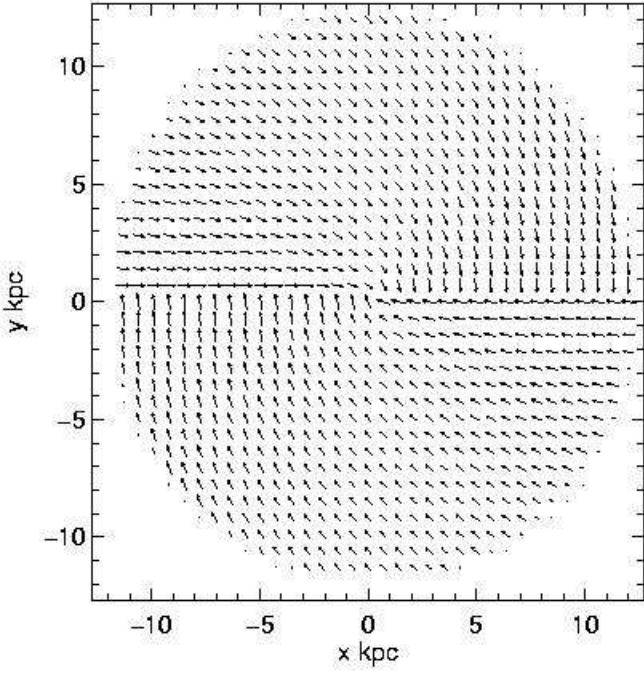


Fig. 17. The configuration of the magnetic field used to explore the effects of geometry and beam smoothing. The bar is located at $y = 0$.

towards the observer. The mid-plane horizontal magnetic field ($\overline{B}_r, \overline{B}_\phi$) is shown in Fig. 17 and is defined as:

$$\overline{B}_r = \begin{cases} -B_0(z)\phi/\pi, & 0 < \phi \leq \pi, \\ B_0(z)(1 - \phi/\pi), & \pi < \phi \leq 2\pi, \end{cases}$$

$$\overline{B}_\phi = \begin{cases} B_0(z)(\phi/\pi - 1), & 0 < \phi \leq \pi, \\ B_0(z)(\phi/\pi - 2), & \pi < \phi \leq 2\pi, \end{cases}$$

$$\overline{B}_z = 0.$$

The dependence of the modelled field on z is described by

$$B_0(z) \propto \exp(-|z|/h_B) \quad (1)$$

with the assumed scale height $h_B = 4$ kpc.

A z -dependent distribution of the form (1) is adopted for thermal electron number density n_e , with the h_B replaced with $h_e = 1$ kpc and the radial distribution truncated at $r = 12$ kpc. The number density of cosmic rays is assumed to be uniform and the synchrotron spectral index is assumed to be $\alpha_s = -1$. After rotating the major axis position angle and inclining the galaxy to the line of sight by the same angles as in the galaxies NGC 1097 and NGC 1365, we calculate the Stokes parameters Q and U by integrating emission along the line of sight over the intervals $\pm 2h_B$ centred at the galaxy's midplane. We convolve the result with a Gaussian of FWHM $10''$ and $15''$ in the plane of the sky for NGC 1097 and NGC 1365, respectively. Depolarization occurs due to differential Faraday rotation along the line of sight and due to beam smearing. Figures 18 and 19 show the obtained synthetic polarized intensity in grey scale with apparent polarization

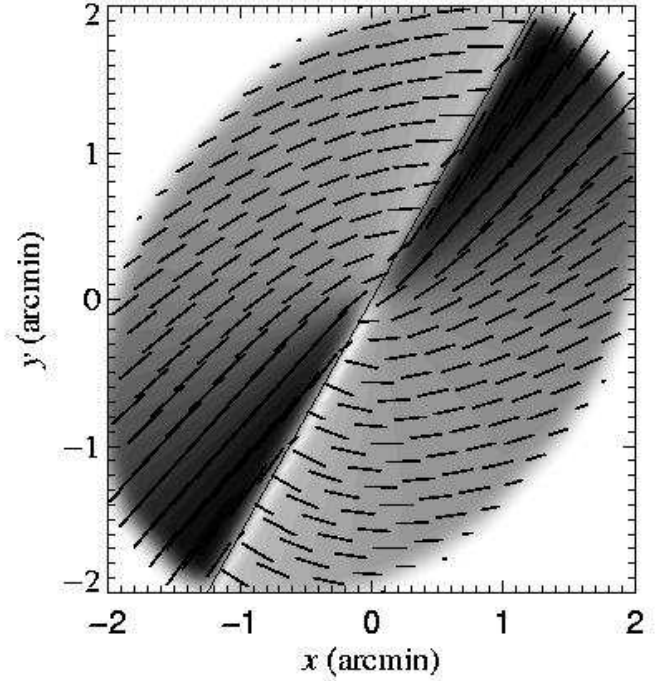


Fig. 18. Synthetic map obtained by rotating the field shown in Fig. 17 with the vertical dependency given by Eq. (1) to the orientation of NGC 1097. The cosmic ray electron distribution is assumed to be uniform and the Stokes parameters Q and U are integrated along all lines of sight, prior to smoothing with a Gaussian beam of FWHM $10''$. The grey scale shows polarized intensity in arbitrary units (with darker shades corresponding to larger values), and the vectors represent the orientation of the polarization plane. The continuous solid line shows the bar major axis.

B -vectors superimposed. Not surprisingly, the abrupt turn of magnetic field by 90° results in strips of small polarized intensity, similar to the depolarization valleys discussed in (Sect. 3.3).

The combination of inclination and smoothing to the beam resolution leads to valleys in P parallel to the bar's major axis which are offset by $15''$ from the ridge of maximum P , consistent with the observations (Sect. 3.3). The width of the valleys of one Gaussian FWHM is also consistent with the observations. Because of the inclination of the galaxies, the two valleys in each model are not equally deep, but the difference is unimportant compared with the intrinsic asymmetries found in the observations. The B -vectors turn by about 90° in front of the bar, much more sharply than in the observations, especially in NGC 1365. This implies that the turn of magnetic field near the depolarization valley in real galaxies is smoother than that in this model, and so it is *partially* resolved in our observations.

We conclude that the effects of disc inclination and beam smoothing can explain the observed offset of the “depolarization valleys” from the ridges, but the observed

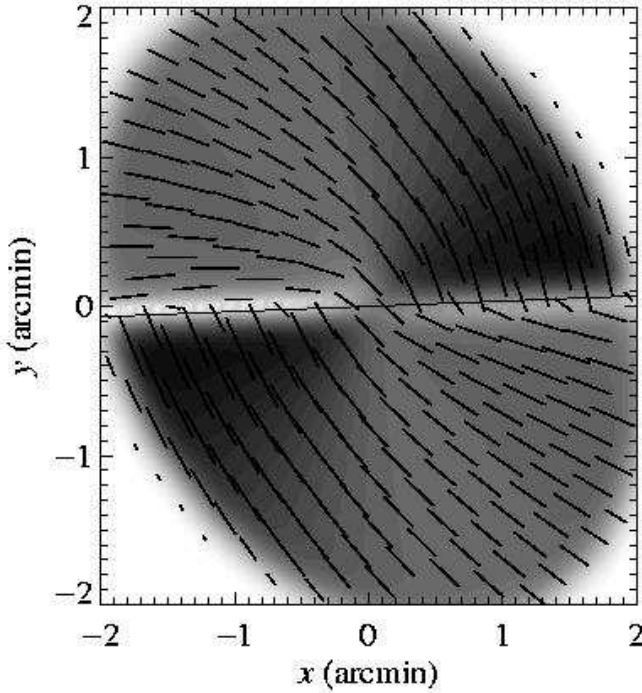


Fig. 19. Same as Fig. 18, but for the inclination and major axis orientation of NGC 1365 and a Gaussian beam of FWHM $15''$.

turning of the B -vectors is much smoother than that predicted from our simple model.

7.2. Misalignment between the velocity field and the magnetic field

As demonstrated above, the smooth deflection of the regular magnetic field cannot be the effect of an intrinsically sharp field reversal, observed with limited resolution in an inclined galaxy, and thus must have a physical reason.

The velocity field of the dense gas in the bar sharply changes its direction in the bar which leads to a shock (Fig. 20). The smooth turning of the observed B -vectors signifies a *misalignment between the velocity field and the magnetic field orientation*. This may imply that the magnetic field diffusivity is significant. The magnetic field may also decouple from the flow of molecular gas, as discussed in Sect. 8.2.3.

The dynamo model of Moss et al. (2001) predicts significant misalignment (by 20 – 45°) in the bar region (see their Fig. 7). A similar conclusion follows from a dynamo model for NGC 1365 (Moss et al. 2005). The misalignment is a strong indication that the regular magnetic field is not frozen into the flow but rather subject to significant diffusion. Then the magnetic field can persist on a 10^9 yr timescale only if supported by dynamo action (cf. Moss et al. 2001).

8. Magnetic field compression and shearing in the radio ridge of NGC 1097

Here we aim to interpret the observed change in the total (I) and polarized (P) radio intensities at the radio ridges described in Sect. 3.2. In Table 3 we calculated that the contrast in I is $\epsilon_I \simeq 5$ – 10 and in P , $\epsilon_P \simeq 1$ – 7 , where the ranges reflect the variation with decreasing distance from the galactic centre. First, we estimate how shock compression and shearing of the total magnetic field (dominated by the turbulent part) is likely to increase I . Then we consider how compression and shear act to change the regular field and hence P . We shall also estimate the contribution to P of the anisotropic random field produced from an isotropic one by compression and shearing.

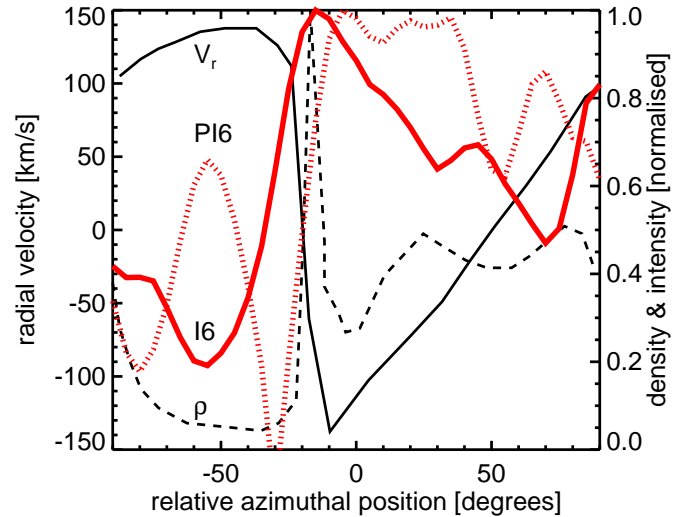


Fig. 20. A cut perpendicular to the bar shock front showing radial velocity (labelled V_r ; thin, black solid), gas density (ρ ; thin, black dashed), total (I6; thick, grey/red solid) and polarized (PI6; thick, grey/red dotted) radio intensities at $\lambda 6$ cm. The radial velocity and density of the gas are from Fig. 10 of Athanassoula (1992b) and are derived from a generic model of a barred galaxy. The azimuthal flow is directed from left to right. The radio data are for the southern end of the bar in NGC 1097 and are average values for a ring at $30''$ (2.5 kpc) radius and $15''$ width. The two data sets (model and observations) have been aligned using the peak in gas density and the peak (ridge) in total radio intensity, defining the zero point of the x -axis. Note that this zero point is different from that used in Fig. 12.

We treat the region of the dust lanes along the bar's leading edge as a shock front where, in addition to compression, velocity shear results from strong flow towards the galaxy's centre behind the shock (Fig. 22). We note that the offset of the dust lanes towards the leading edge of the bar is a sign of a strong shear shock in the velocity field (Athanassoula 1992b). Thus, the magnetic field is compressed and sheared at the shock front. Each effect

not only amplifies the magnetic field, but also makes its turbulent part anisotropic.

Figure 20 shows a perpendicular slice through the bar region using radial velocity and gas density data from the model of Athanassoula (1992b) and our radio data from NGC 1097.

We have aligned the two datasets by the peaks in gas density and total radio intensity. Figure 20 illustrates the general interpretation of the radio ridges that is developed below; compression and shear produce stronger total and polarized intensities. The depolarized valley (at -30° relative azimuthal position in Fig. 20) and the strong upstream polarized intensity (at -50°) are also clearly visible.

We assume that the gas speed normal to the shock immediately behind it is comparable to the sound speed (Roberts et al. 1979, Englmaier & Gerhard 1997) and we adopt a sound speed of $c_s = 10 \text{ km s}^{-1}$; if the velocity normal to the shock is subsonic (e.g. Roberts et al. 1979), the arguments presented below are either strengthened or unaffected. In order to simplify our estimates, we assume that the shock front is in the vertical plane passing through the galactic rotation axis (thus neglecting the offset of the front from the bar’s major axis – e.g., Athanassoula 1992b), so that magnetic field components normal and tangent to it are $B_n = B_\phi$ and $B_t = (B_r, B_z)$, where (r, ϕ, z) are cylindrical polar coordinates in the galaxy’s frame, centred at the galaxy’s centre.

8.1. Contrast in total radio intensity

In order to estimate the compression ratio (the ratio of post- to pre-shock values) of the total synchrotron intensity, ϵ_I , we assume that the contribution of the regular magnetic field to the total field is negligible at the required level of accuracy, as indicated by our observations. In Sect. 3.6 we estimated the strength of the regular field in the ridges as about $2 - 4 \mu\text{G}$ while the total field is about $25 \mu\text{G}$ (Table 3).

In Appendix A we derive two equations for ϵ_I when an initially isotropic, random magnetic field is subject to shock compression and shear. Equation (A.6) applies when the cosmic ray electron density is not changed by the shock (at least, on the scale of our resolution of about 500 pc) whereas Eq. (A.7) includes the common assumption that the energy density of cosmic rays is equal to the energy density of the magnetic field – in this case the synchrotron emission is enhanced both by an increase in field strength and an increase in cosmic ray electron density. Figures 21(a) and 21(b) show how ϵ_I depends on the compression ratio of the gas density, ϵ_ρ , for different magnitudes of the velocity shear, parameterized by the factor K .

The most striking difference between the constant cosmic ray density and the equipartition cases is an order of magnitude higher contrast in synchrotron emission predicted by the equipartition model. For a shear strength of

$K = -2$ (see Appendix A) and the gas density contrast of an adiabatic shock $\epsilon_\rho = 4$, the model using constant cosmic ray density (Fig. 21(a)) predicts $\epsilon_I \simeq 10$, as observed in the inner bar of NGC 1097 and NGC 1365 (Table 3). Note that, although Fig. 21 is plotted using the geometrical parameters of NGC 1365, the different inclination and bar position angle of NGC 1097 produce similar, but not identical, results. The lower observed values of ϵ_I at larger radii can be attributed to weaker shear, a weaker shock or a combination of both. In order for the equipartition model (Fig. 21(b)) to match the observed ϵ_I requires both a much weaker velocity shear $K \simeq -1$ and a small increase in gas density $\epsilon_\rho \simeq 2$. Since the velocity and gas density fields of these galaxies are not known to a sufficient accuracy to allow a confident rejection of one of the models, we can only note that with a constant cosmic ray density, a far greater range of parameters describing the shock and shear are compatible with the observed ϵ_I , whereas equipartition requires both weak shear and low compression.

We conclude that the observed enhancement of total radio intensity in the radio ridges is consistent with amplification of the random magnetic field by shock compression and shear. Better observational data on the gas density (CO and H I) and velocity fields in the bars of NGC 1097 and NGC 1365 may provide a novel way in which to test the assumption of energy density equipartition between cosmic rays and magnetic fields.

8.2. Contrast in polarized intensity

Polarized intensity (P) can be increased in the radio ridge due to (i) shock compression and shearing of the turbulent field producing an anisotropic turbulent magnetic field as described above and (ii) compression and shearing of the regular magnetic field. These effects will tend to align the magnetic field with the shock front and so a strong increase in P can be expected.

8.2.1. Polarization from an anisotropic turbulent magnetic field

Equation (A.8) gives the degree of polarization produced by a compressed and sheared random magnetic field. This equation assumes that the cosmic ray density is constant. We have not derived a version for the case of energy density equipartition between cosmic rays and magnetic field, but it is sufficient for the present purposes to note that equipartition will tend to increase the degree of polarization as discussed in Sect. 5.2 of Sokoloff et al. (1998).

Figure 21(c) shows the degree of polarization, assuming $p_0 = 0.7$ for the intrinsic polarization, for the geometry of NGC 1365 as a function of ϵ_ρ for different shear strengths. Again, the case of NGC 1097 is slightly, but not significantly different. In the absence of compression ($\epsilon_\rho = 1$), increasing the shear produces a greater degree of polarization by producing stronger anisotropy. With in-

creasing compression the degree of polarization converges to $p \simeq 0.5$, regardless of the shear. However, for the strongest shear shown, with $K = -8$, the behaviour is counter-intuitive: stronger compression *reduces* the degree of polarization. This happens because the vertical component of the random magnetic field, b_z , is increased by compression together with b_r . The projection of the stronger b_z into the sky plane has components parallel *and orthogonal* to the sheared b_ϕ , thus reducing the anisotropy of \mathbf{b}_\perp . We have confirmed this explanation by re-deriving Eq. (A.8) with $b_z = 0$: in this case, no matter how large $|K|$ is, the slope of p is never negative.

For $\epsilon_\rho = 4$, the degree of polarization arising from anisotropic turbulent magnetic field is $p \simeq 0.5$ in NGC 1365 and $p \simeq 0.4$ in NGC 1097, with only a weak dependence on the shear strength. These are *overestimates* since we do not include any beam depolarization. Nevertheless, the expected degree of anisotropy of the turbulent magnetic field is rather high and should contribute significantly to the observed polarized intensity.

The above estimate is based on the anisotropy in \mathbf{b} immediately behind the shock, as specified in Eq. (A.1). In fact the isotropy of the turbulent magnetic field can be restored rather quickly if the turbulence forcing is isotropic. With standard estimates of the turbulent eddy size of $l = 100$ pc and the turbulent velocity $v = 10$ km s $^{-1}$, the magnetic field can return to isotropy in the eddy turnover time $\tau = l/v \simeq 10^7$ yr. Given that, behind the shock, the gas speed normal to the shock is equal to the speed of sound $c_s \simeq 10$ km s $^{-1}$ (Roberts et al. 1979, Englmaier & Gerhard 1997; see above) and the width of the radio ridge is $d \simeq 500$ pc, the residence time of the gas in the ridge is $\tau_r \simeq d/c_s \simeq 5 \times 10^7$ yr, which exceeds the isotropization time severalfold. Hence the degree of anisotropy estimated above only applies to a region in the close vicinity of the shock front and may be lower when averaged over our $6'' \simeq 500$ pc telescope beam. Thus, whilst shock compression of the turbulent magnetic field will give rise to a strong increase in I (see Sect. 8.1) it may only have a weaker effect on P .

8.2.2. Polarization from a sheared regular magnetic field

Now we consider the effect of shear in the velocity field on the regular (coherent) magnetic field. Gas-dynamical simulations (e.g., Fig. 10 of Athanassoula 1992b; see also Fig. 20 here) confirm that the radial velocity in the dust lane region changes very rapidly near the ridge, from an outward to an inward direction, and subsequently varies slowly. If the radial velocity changes by ΔV_r over the dust lane of a width d , the radial magnetic field \overline{B}_r produced from the azimuthal one \overline{B}_ϕ by the shear is

$$\overline{B}_r \approx \overline{B}_\phi \frac{\Delta V_r}{d} \tau_r \simeq \overline{B}_\phi \frac{\Delta V_r}{c_s} \simeq 10 \overline{B}_\phi, \quad (2)$$

where $\tau_r \simeq d/c_s$ is the residence time in the shock region, $\Delta V_r \simeq 100$ km s $^{-1}$ and $c_s \simeq 10$ km s $^{-1}$. The enhancement

of the magnetic field tangent to the shock front by compression is $\epsilon_B \simeq 4$ for an adiabatic shock. This is a factor of more than two smaller than the amplification by shear, Eq. (2). In addition, the regular magnetic field is almost perpendicular to the shock upstream of it, which reduces the effect of compression and enhances the effect of shear. So, we neglect the compression of the regular magnetic field.

A similar estimate of regular field amplification in the ridge follows from the observed deflection of the polarization plane discussed in Sect. 3.3, where we note that magnetic pitch angles upstream and downstream of the shock front in NGC 1097 are $p_{A1} \simeq 15^\circ$ and $p_{A2} \simeq 75^\circ$, respectively. Given that $\overline{B}_r/\overline{B}_\phi = \tan p_A$ and $\overline{B}_{\phi1} \approx \overline{B}_{\phi2}$, since the azimuthal field component is nearly normal to the shock front, we obtain $\overline{B}_{r2}/\overline{B}_{r1} \approx \tan p_{A2}/\tan p_{A1} \simeq 14$, which is in fair agreement with Eq. (2).

Such an enhancement of the regular magnetic field must result in a very significant increase in polarized intensity. The enhancement factor of polarized emissivity can be estimated using Eqs. (A.4) and (A.5), but now written for the components of the transverse (i.e. in the plane of the sky) regular magnetic field $\overline{\mathbf{B}}_\perp = (\overline{B}_{x'}, \overline{B}_{y'})$. Assuming for the sake of simplicity that, in the galaxy's plane, the regular magnetic field is purely azimuthal in front of the shock, $\overline{\mathbf{B}}_1 = (0, \overline{B}_\phi, 0)$, and purely radial behind it, $\overline{\mathbf{B}}_2 = (\overline{B}_r, 0, 0)$, and that the enhancement factor in polarized synchrotron emissivity $\epsilon_{P2}/\epsilon_{P1}$ is equal to that in \overline{B}_\perp^2 (i.e., the energy density of cosmic rays is constant across the shock), we obtain

$$\begin{aligned} \epsilon_P &= \frac{\epsilon_{P2}}{\epsilon_{P1}} \\ &= \left(\frac{\Delta V_r}{c_s} \right)^2 \frac{1 - \cos^2 \phi \sin^2 i}{1 - \sin^2 \phi \sin^2 i} \\ &\simeq \begin{cases} 60 & \text{in NGC 1097,} \\ 90 & \text{in NGC 1365.} \end{cases} \end{aligned} \quad (3)$$

If the region with strong shear is not resolved then the increase in polarized emission can be smaller than this. However, in order to achieve $\epsilon_{P,\text{obs}} \simeq 3$ (Table 3) would require the width of the sheared region to be about $d \simeq W \epsilon_{P,\text{obs}}/\epsilon_P \simeq 50$ pc in NGC 1365 (where $W = 1.5$ kpc is the beamwidth) and even less in NGC 1097. In addition, the observed ϵ_P does not increase in our maps with higher resolution, so the low observed values are not due to our limited resolution.

We conclude that the observed contrast in polarized intensity is inconsistent with the expected amount of magnetic field enhancement if it is subject to a full amount of shearing in the dust lanes.

8.2.3. Decoupling of the regular magnetic field from the molecular clouds

From the above arguments, it is clear that the combined effects of anisotropic turbulent magnetic field and

sheared regular magnetic field should produce a significant increase in the polarized intensity around the shock front/dust lane. However, we observe only a modest contrast of $\epsilon_P \simeq 0.5\text{--}7$ (Table 3).

The simplest way to resolve the conflict between the expected and observed ϵ_P , without having to abandon our successful description of ϵ_I in Section 8.1, is to suggest that the regular magnetic field resists shearing by the radial velocity field. As we argue in what follows, this can happen if *the regular magnetic field becomes decoupled from the dense gas (molecular clouds) in the shocked region*. A typical time scale for the formation of H_2 molecules is of order 10^6 yr (Jura 1975, Bergin et al. 2004), much less than the residence time in the ridge $\tau_r \simeq 5 \times 10^7$ yr. As molecular clouds form, it is plausible that they become detached from the regular magnetic field, carrying with them and amplifying only the random, small-scale magnetic field. One mechanism (Ohmic diffusion) has already been proposed for this process by Mestel & Strittmatter (1967) and others are plausible, such as ambipolar diffusion and reconnection of the external field as a forming cloud rotates; further discussion is beyond the scope of this paper (see Fletcher & Shukurov 2005).

In order for the regular field – and hence the polarized intensity – not to be increased as strongly as suggested by Eq. (3), it must be sufficiently strong to prevent the diffuse gas, to which it is coupled, from being sheared. Consider a shear flow $\mathbf{V} = (V_x(y), 0, 0)$ with a horizontal magnetic field embedded into it, $\mathbf{B} = (\overline{B}_x, \overline{B}_y, 0)$, where the x -axis is parallel to the radial direction and the y -axis is directed along azimuth. The magnetic braking of the radial shear flow is controlled by the x -component of the Navier–Stokes equation,

$$\frac{\partial V_x}{\partial t} \simeq \frac{1}{4\pi\rho} \overline{B}_y \frac{\partial \overline{B}_x}{\partial y}, \quad (4)$$

where we have neglected the x -derivative of magnetic field in comparison with its y -derivative. For simplicity, consider the effect on the magnetic field of compression alone. This will result in a very conservative estimate of the effect of magnetic field on the flow since additional amplification by the shear is neglected. Thus, \overline{B}_x is compressed over a length d_1 by a factor ϵ_ρ , whereas \overline{B}_y remains unchanged: $\partial \overline{B}_x / \partial y \simeq (\epsilon_\rho - 1) \overline{B}_x / d_1$. Since the azimuthal speed behind the shock is close to the speed of sound c_s (see above), the increment in the radial velocity produced by magnetic stress over a length d_2 follows as

$$\begin{aligned} \Delta V_x &\simeq \frac{\epsilon_\rho - 1}{c_s} \frac{\overline{B}_x \overline{B}_y}{4\pi\rho} \frac{d_2}{d_1} \\ &\simeq 70 \frac{\text{km}}{\text{s}} \left(\frac{\overline{B}_x \overline{B}_y}{10 \mu\text{G}^2} \right) \left(\frac{n}{0.2 \text{ cm}^{-3}} \right)^{-1} \left(\frac{c_s}{10 \text{ km s}^{-1}} \right)^{-1}, \end{aligned} \quad (5)$$

where the numerical value has been obtained for $d_1 = d_2$ and $\epsilon_\rho = 4$. We have the following additional constraints:

$$\begin{aligned} \overline{n}_e \overline{B}_\parallel &\simeq 0.3 \mu\text{G cm}^{-3}, \\ \overline{n}_e^2 L &\simeq 100 \eta \text{ cm}^{-6} \text{ pc}, \\ \overline{n}_e &= X \overline{n}, \end{aligned} \quad (6)$$

where the first is derived from Faraday rotation values in the ridge (Sect. 3.4), the second from the estimated EM with η the filling factor of the diffuse ionised gas (Sect. 3.6), and the third defines the degree of ionisation X of the diffuse gas. For the inclination of NGC 1097 and NGC 1365, $L \simeq 2\sqrt{2}h$ where h is the scale height of the diffuse gas. Combining Eq. (5), with $\overline{B}_x = \overline{B}_y = \overline{B}/\sqrt{2}$, $\Delta V_x = 100 \text{ km s}^{-1}$ and $c_s = 10 \text{ km s}^{-1}$, and Eqs. (6) we obtain expressions for the regular magnetic field strength, diffuse gas density and the scale height of the ionized layer in terms of the least well known parameters η and X :

$$\begin{aligned} \frac{\overline{B}}{1 \mu\text{G}} &\simeq 4X^{-1/3}, \\ \frac{\overline{n}}{1 \text{ cm}^{-3}} &\simeq 0.1X^{-2/3}, \\ \frac{h}{1 \text{ kpc}} &\simeq 3\eta X^{-2/3}. \end{aligned} \quad (7)$$

In other words, Eq. (5) – and hence the suppression of shear in the diffuse gas – is consistent with the observed RM and EM and the assumed disc thickness if Eqs. (7) give reasonable values of \overline{B} , \overline{n} and h , using the chosen fractional ionisation X and the diffuse gas filling factor η . This is the case for $X \gtrsim 0.5$ and $\eta \lesssim 0.2$, plausible values for both parameters. For example, $X = 0.5$ and $\eta = 0.2$ gives $\overline{B} \simeq 5 \mu\text{G}$, $\overline{n} \simeq 0.2 \text{ cm}^{-3}$ and $h \simeq 1 \text{ kpc}$. The latter is similar to the scale height of the diffuse gas in the Milky Way (Reynolds 1990) and the filling factor $\eta = 0.2$ is similar to that of the diffuse thermal electrons in normal spiral galaxies (Greenawalt et al. 1998).

To summarise this section: the increase in polarized intensity in the ridge, with respect to the upstream region, is much lower than expected because the regular magnetic field decouples from the dense molecular gas clouds and is sufficiently strong to prevent shearing and compression in the diffuse ionised gas. The regular magnetic field of about $5 \mu\text{G}$ in strength can be *dynamically important in the diffuse gas* of density $\approx 0.2 \text{ cm}^{-3}$. If the ionization degree of the diffuse gas is of order 50% and the scale height of the diffuse ionised gas is about 1 kpc, the resulting emission measure is compatible with that observed in the southern ridge of NGC 1097.

8.3. Variation in RM across the dust lane

The variation of the Faraday rotation measure across the inner southern radio ridge region of NGC 1097 (left-hand panel of Fig. 12) is unusual. The discontinuous change in sign of rotation measure arises because the radial component of the regular magnetic field changes direction across the shock front. This counter-intuitive arrangement of magnetic field directions is confirmed by the fitting of the large-scale polarization structure with azimuthal Fourier modes presented in Sect. 4. Figure 22 illustrates how such a magnetic field configuration can be produced by a shear shock. We should remember that the observed polarization vectors are dominated by the anisotropic field

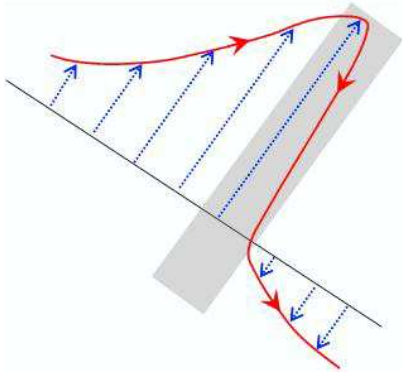


Fig. 22. An illustration of the shearing of the regular magnetic field in the radio ridges. The orientation of the figure and the field direction roughly correspond to those in the southern part of NGC 1097. A magnetic line shown with continuous line is sheared by a velocity field component along the radio ridge (dust lane) region, whose vectors are indicated with dotted lines; the thin straight line shows the orientation of the original magnetic field; the unresolved part of the system is shown shaded.

which is strictly aligned along the shock front. The sheared regular field sketched in Fig. 22, visible only in Faraday rotation, is tilted with respect to the shock front.

The sharp change in magnetic field orientation at the sheared region (Fig. 22) explains the origin of the depolarized valley: If the region of strongest shearing is narrow compared to the beam (as we argued in Sect. 8.2.2), then the almost orthogonal field orientations will give rise to strong, wavelength-independent beam depolarization. A shift of the polarization ridge downstream with respect to the total intensity ridge will also result, as observed (Sect. 3.2).

9. Mass inflow through the nuclear ring of NGC 1097

The nuclear ring of NGC 1097 is a site of intense star formation with a rate of $5M_{\odot} \text{ yr}^{-1}$ (Hummel et al. 1987) and, presumably, strong gas inflow to fuel the central activity. Beck et al. (1999) suggested that the stress required to drive the inflow into the central region can be provided by the magnetic field. The total magnetic field in the nuclear ring and its regular + anisotropic random part are estimated, from equipartition arguments, to be $B_I \simeq 50\text{--}60 \mu\text{G}$ and $B_P \simeq 10\text{--}20 \mu\text{G}$, respectively (Table 4). The regular magnetic field has the form of a trailing spiral with a pitch angle of $p_A \simeq 40^\circ$. This field produces the $r\phi$ -component of the stress tensor $T_{r\phi} = -\overline{u_A r u_{A\phi}}$, where $\mathbf{u}_A = \mathbf{B}/(4\pi\rho)^{1/2}$ is the Alfvén velocity based on the total magnetic field.

The accretion rate driven by this stress is $\dot{M} = 2\pi\sigma\Omega^{-1}T_{r\phi}$, where $\sigma \simeq 2h\rho$ is the gas surface density,

with $2h$ the disc thickness, and Ω is the angular velocity of the gas (e.g., Balbus & Hawley 1998). This yields

$$\dot{M} \simeq -\frac{h}{\Omega}(\overline{b_r b_\phi} + \overline{B_r B_\phi}), \quad (8)$$

where \mathbf{b} and \mathbf{B} are the turbulent and regular magnetic field components, respectively, and overbar denotes averaging – cf. Eq. (4).

With $c = \overline{b_r b_\phi}/\overline{b^2}$, we obtain

$$\begin{aligned} \dot{M} &\simeq -\frac{h}{\Omega}(c\overline{b^2} + \frac{1}{2}\overline{B^2} \sin 2p) \\ &\simeq -c M_{\odot} \text{ yr}^{-1}, \end{aligned}$$

where $c \simeq -1$ is a numerical factor (see below) and the estimate has been obtained for $h = 0.1 \text{ kpc}$, $\Omega = 450 \text{ km s}^{-1} \text{ kpc}^{-1}$, $\overline{b^2}^{1/2} = 50 \mu\text{G}$, $\overline{B} = 10 \mu\text{G}$ and $p_A = 40^\circ$; we have retained only the (dominant) first term in Eq. (8). Hence, we derive a mass inflow rate of a few $M_{\odot} \text{ yr}^{-1}$ which is sufficient to feed the active nucleus.

A correlation between the azimuthal and radial components of the turbulent magnetic field used above arises from the shearing of turbulent magnetic field by differential rotation. From arguments similar to those used to obtain Eq. (A.3) and assuming that the relevant turbulent timescale is h/c_s (as in accretion discs) we obtain

$$b_\phi = r \frac{d\Omega}{dr} \frac{h}{c_s} b_r \simeq -\frac{q\Omega h}{c_s} b_r, \quad (9)$$

where the rotation curve is assumed to be of the form $\Omega \propto r^{-q}$, with $q = 1$ corresponding to a flat rotation curve. Assuming that $\overline{b_r^2} = \frac{1}{3}\overline{b^2}$, we obtain $c = \overline{b_r b_\phi}/\overline{b^2} \simeq -\frac{1}{3}q\Omega h/c_s$.

The problem of mass transport from a circumnuclear ring into an active nucleus has been addressed by many authors (see review by Knapen 2004). The inflow rate due to magnetic stress is much larger than that normally produced by gravitational torques in the nuclear ring (Maciejewski et al. 2002). We note that turbulent stress can result in a similar inflow rate given that magnetic field and turbulence are in energy equipartition. Strong magnetic fields are known to exist in the centres of most galaxies from the observation of strong synchrotron emission. Hence magnetically driven inflow can be important not only in barred galaxies, but also in normal spiral galaxies with a magnetized inner disc (Moss et al. 2000).

10. Summary and conclusions

- We have detected polarized emission in the galaxies NGC 1097 and NGC 1365 which gives important information about the interaction of the gas flow and the magnetic field structure in barred galaxies.
- The total magnetic field is strong in the central star-forming regions of NGC 1097 and NGC 1365 (about $60 \mu\text{G}$) and in the radio ridges along the galaxies' bars ($20\text{--}30 \mu\text{G}$).

- In both galaxies, the magnetic field orientation changes strongly, but smoothly in front of the radio ridges. This causes a valley of depolarization where the polarized emission almost vanishes. The smooth deflection of the magnetic field is different from that of the (likely) velocity field of the dense gas which changes its direction abruptly.
- The enhancement of total radio intensity in the radio ridges along the bars of NGC 1097 and NGC 1365 can be explained by shock compression and shearing of the isotropic random field, together with compression of the gas, by a factor of about 4 and constant cosmic ray density across the shock. Local equipartition conditions, where the cosmic rays are compressed together with the magnetic field, are hardly compatible with our data as they require both low compression and low shear.
- The enhancement of polarized intensity is much lower than that of the total synchrotron intensity. *The regular magnetic field resists shearing because it is decoupled from the dense gas*, and the Maxwell stress is sufficient to oppose efficiently the development of a shear flow developing in the diffuse gas to which the regular magnetic field remains coupled. This also contributes to the misalignment between the magnetic field and the velocity field of the dense gas in front of the ridges.
- The enhanced polarized emission in the ridges can be explained by the presence of anisotropic random fields due to compression of isotropic random fields in the shock. These anisotropic fields dominate over the regular (coherent) fields which are visible through their Faraday effects.
- Faraday rotation measures reveal jumps across the ridge, where the amplitude decreases with increasing distance from the galaxy's centre. This behaviour results from shearing of the regular field.
- We have demonstrated that radio continuum data of the total and polarized emission form a new and powerful tool to determine the shock strength and the shear rate in the shearing shocks of barred galaxies. If the gas compression is known from independent measurements (H I and CO), the validity of energy equipartition between magnetic fields and cosmic rays can also be tested.
- Enhanced polarized intensity ahead of the shock fronts of NGC 1097 and NGC 1365, at several kpc distance from the bar, could be a signature of regular fields generated by dynamo action. Alternatively, compression of gas and magnetic fields may occur in the region of narrow dust filaments visible on optical images. The magnetic field is aligned with these filaments.
- Magnetic braking in the circumnuclear regions of galaxies is a fundamental process which may solve the long-standing problem of how to feed active galactic nuclei. We have shown that the magnetic fields in the circumnuclear ring of NGC 1097 are sufficiently strong ($\simeq 60 \mu\text{G}$) to drive a mass inflow of several $M_{\odot} \text{ yr}^{-1}$.

- X-ray emission in NGC 1097, detected with ROSAT, reveals hot gas (of a temperature about 10^7 K) in the central region and also an extended hot gas component. A crude estimate of the electron density in the extended component yields $n_e \simeq 3.4 \times 10^{-3} \eta^{-1/2} \text{ cm}^{-3}$ (where η is the volume filling factor of the hot gas). If the extended X-ray and the extended radio components both emerge from a halo and $\eta \simeq 0.3$, the derived thermal energy density of the hot gas is comparable to the energy density of the magnetic field. A more detailed spectral and spatial X-ray analysis to study further the hot gas in the ISM of barred galaxies such as NGC 1097 requires deep observations at high throughput observatories like XMM-Newton.

Acknowledgements. We are grateful to Lia Athanassoula who kindly provided data from her gas-dynamical models for barred galaxies. We thank Elly M. Berkhuijsen and our referee for careful reading of the manuscript and many useful comments. This work was supported by the PPARC grant PPA/G/S/2000/00528, RFBR grant 04-02-16094 and DFG/RFBR grant 96-02-00094G. We have made use of the ROSAT Data Archive of the Max-Planck-Institut für extraterrestrische Physik (MPE) at Garching, Germany.

Appendix A: The effect of compression and shear on a random magnetic field

Here we derive equations describing the increase in total synchrotron emission and polarization resulting from shock compression and shearing of an initially isotropic, random magnetic field. For the total emission we consider two cases: first, and simpler, we assume that the energy density of cosmic ray electrons is constant (i.e. the density of cosmic rays is not affected by the shock); then we present the more complex model where the cosmic rays are in energy equipartition with the magnetic field. Finally, we examine how much polarized emission emerges from the anisotropic field produced by shock compression and shearing.

The component of the random magnetic field tangent to the shock front is compressed together with the gas, whereas the normal component remains unchanged,

$$b_{t2} = \epsilon_{\rho} b_{t1} , \quad b_{n2} = b_{n1} , \quad (\text{A.1})$$

where $\epsilon_{\rho} = \rho_2/\rho_1$ is the density ratio and subscripts 1 and 2 refer to pre- and post-shock values, respectively. We assume for simplicity that the random field is isotropic upstream of the shock,

$$\langle b_{n1}^2 \rangle = \frac{1}{2} \langle b_{t1}^2 \rangle = \frac{1}{3} \langle b_1^2 \rangle , \quad (\text{A.2})$$

where angular brackets denote averaging. Thus, the compressed field is anisotropic, with the dominant components tangent to the shock front.

The anisotropy of the random magnetic field in the postshock region is further enhanced by velocity shear. We introduce cylindrical polar coordinates (r, ϕ, z) and assume for simplicity that the shock is parallel to the r

direction. If the radial velocity changes by ΔV_r across the shock region of a width d , the radial magnetic field b_{r2} produced from the azimuthal $b_{\phi1}$ by the shear is

$$b_{r2} \approx b_{\phi1} \frac{\Delta V_r}{d} \tau_r = b_{\phi1} \frac{\Delta V_r}{v_0} \frac{l}{d} \simeq -2b_{\phi1}, \quad (\text{A.3})$$

where $\tau_r = \min(d/c_s, l/v_0)$ is the relevant amplification time (the minimum of the residence time within the sheared region, d/c_s (where c_s is the sound speed), and the eddy turnover time l/v). Since the turbulent velocity $v_0 \simeq c_s$ and $d > l$, we obtain the second equality in Eq. (A.3), and the third follows for $\Delta V_r = -100 \text{ km s}^{-1}$ (Athanasoula 1992b), $v_0 = 10 \text{ km s}^{-1}$, $d = 500 \text{ pc}$ and $l = 100 \text{ pc}$.

The radial component of the random magnetic field behind the shock thus consists of two parts, the compressed one, denoted by $b_r^{(c)}$ as given in Eqs (A.1) and (A.2), and the sheared part $b_r^{(s)}$ given by Eq. (A.3). Although $\langle b_r b_\phi \rangle \approx 0$ ahead of the shock (if the field anisotropy can be neglected there), the shearing produces correlated field components behind the shock, $\langle b_r b_\phi \rangle = \langle b_r^{(s)} b_\phi \rangle \simeq \langle b_\phi^2 \rangle (\Delta V_r l) / (v_0 d)$ (where $\Delta V_r < 0$). For the post-shock field produced by compression, we have $b_{r2}^{(c)} = \epsilon_\rho b_{r1}$ and likewise for the z -component, whereas the ϕ -component remains unchanged as it is normal to the shock front. The compression enhances an isotropic random magnetic field by a factor of $[\frac{1}{3}(1 + 2\epsilon_\rho^2)]^{1/2}$. For a strong shock ($\epsilon_\rho = 4$) the compression factor is approximately 3.

Since synchrotron intensity depends on the magnetic field component in the plane of the sky, its compression factor ϵ_I depends on the orientation of the shock front with respect to the observer. Appropriate expressions for the magnetic field projection to the plane of the sky, $\mathbf{b}_\perp = (b_{x'}, b_{y'})$, in terms of its cylindrical components $\mathbf{b} = (b_r, b_\phi, b_z)$ in the galaxy's reference frame can be found in Appendix A of Berkhuijsen et al. (1997):

$$b_{x'} = b_r \cos \phi - b_\phi \sin \phi, \quad (\text{A.4})$$

$$b_{y'} = (b_r \sin \phi + b_\phi \cos \phi) \cos i + b_z \sin i, \quad (\text{A.5})$$

where i is the inclination angle of the galactic disc ($i = 0$ corresponds to the face-on view) and ϕ is the azimuthal angle in the galaxy's plane measured anticlockwise from the northern end of the major axis, related to that in the sky plane, ϕ' , by $\tan \phi \cos i = \tan \phi'$. The x' -axis in the sky plane points to the northern end of the galaxy's major axis; here and below, coordinates in the plane of the sky are denoted with primes, (x', y') .

In order to calculate the contrast in synchrotron intensity, we consider the two models described below.

A.1. Total intensity contrast for uniform cosmic ray distribution

If the energy density of cosmic rays does not vary across the radio ridge (i.e., at a scale of 1 kpc), the increase in synchrotron emission depends solely on the change in

b_\perp , the magnetic field component parallel to the plane of the sky, and any variation in the disc thickness between the shocked and upstream region. Then Eqs. (A.1), (A.2) and (A.3) yield the contrast in total synchrotron intensity between the shocked and upstream regions:

$$\begin{aligned} \epsilon_I &= \frac{\langle b_{\perp 2}^2 \rangle}{\langle b_{\perp 1}^2 \rangle} \frac{L_2}{L_1} \\ &= \frac{1}{2} \frac{L_2}{L_1} [2 + (\epsilon_\rho^2 + K^2 - 1)(1 + \sin^2 i \cos^2 \phi) \\ &\quad - K(K + \sin 2\phi) \sin^2 i], \end{aligned} \quad (\text{A.6})$$

where $K = (\Delta V_r l) / (v_0 d)$ is a measure of the strength of the shear and for the canonical values given above $K \simeq -2$. We have assumed that different components of the compressed part of \mathbf{b} remain statistically independent, $\langle b_r^{(c)} b_\phi \rangle = 0$ and similarly for the other components. For $L_1 = L_2$, $\epsilon_\rho = 1$ and $\Delta V_r = 0$, we obtain, as it should be, $\epsilon_I = 1$; for $i = 0$ (the face-on view), the contrast in I becomes independent of azimuth.

A.2. Total intensity contrast under energy equipartition between cosmic rays and magnetic fields

Here we consider the case where the energy density of cosmic rays is proportional to the energy density of the total magnetic field. Then the synchrotron emissivity behind the shock will be increased both because of the field amplification by compression and shear and, additionally, due to the accompanying increase in the cosmic ray electron density where $n_{\text{cr}} \propto b^2$. Now we obtain, for $L_1 = L_2$:

$$\begin{aligned} \epsilon_I &= \frac{\langle b_{\perp 2}^2 b^2 \rangle}{\langle b_{\perp 1}^2 b^2 \rangle} \\ &= 1 + \frac{3}{10} (\epsilon_\rho^2 + K^2 - 1)^2 (\cos^2 i + \cos^2 \phi \sin^2 i) \\ &\quad + \frac{1}{10} (\epsilon_\rho^2 + K^2 - 1) (4 + 9 \cos^2 i + 7 \cos^2 \phi \sin^2 i) \\ &\quad + \frac{1}{10} (\epsilon_\rho^2 - 1) (\epsilon_\rho^2 + K^2 - 1) (1 + \cos^2 \phi \sin^2 i) \\ &\quad + \frac{1}{10} (\epsilon_\rho^2 - 1) (3\epsilon_\rho^2 + 4) \sin^2 i \\ &\quad - \frac{1}{10} K (1 + \epsilon_\rho^2 + K^2) \sin 2\phi \sin^2 i, \end{aligned} \quad (\text{A.7})$$

following careful treatment of the averages of the components of the field and their cross terms ($\langle b_r^4 \rangle$, $\langle b_r^2 b_\phi^2 \rangle$ etc.) and some algebra.

A.3. Polarization from an anisotropic random magnetic field

For a uniform cosmic ray distribution, we will now derive the degree of polarization from the anisotropic random magnetic field created by the combined effects of compression and velocity shear in the shock.

An anisotropic random field in the plane of the sky, $\mathbf{b}_t = (b_{r'}, b_{z'})$, produces a degree of polarization (Sokoloff et al. 1998):

$$p = p_0 \left| \frac{\langle b_{t2'}^2 \rangle - \langle b_{n2'}^2 \rangle}{\langle b_{\perp 2}^2 \rangle} \right| \equiv p_0 \left| \frac{C_1}{C_2} \right|, \quad (\text{A.8})$$

where

$$\begin{aligned}
C_1 &= \frac{1}{4}(\epsilon_\rho^2 + K^2 - 1) \\
&\times \left[(1 - \cos i)^2 \cos 4\phi - 2 \cos 2\phi \sin^2 i + (1 + \cos i)^2 \right] \\
&\quad + K^2 \cos 2\phi \sin^2 i - \frac{1}{2}K \sin 4\phi (1 - \cos i)^2, \\
C_2 &= 2 + (\epsilon_\rho^2 + K^2 - 1)(1 + \sin^2 i \cos^2 \phi) \\
&\quad - K(K + \sin 2\phi) \sin^2 i,
\end{aligned}$$

and $p_0 \approx 0.7$ is the maximum degree of polarization.

The observed degree of polarization depends on the position in the galaxy because of projection effects. As expected, the observed degree of anisotropy of the magnetic field components in the sky plane behind the shock is independent of azimuth ϕ (together with p) for face-on view $i = 0$. The observed anisotropy is maximum when the shock occurs at the minor axis $\phi = 90^\circ$ and zero at the major axis $\phi = 0$ when the disc is viewed edge-on, $i = 90^\circ$.

Appendix B: Parameters of the fitted regular magnetic fields

In Tables B.1 and B.2 we give the parameters of the fitted regular magnetic field models discussed in Section 4. Although a component of the regular field perpendicular to the disc plane (B_z in Eq. (B.2)) is allowed in the model and we searched for fits using this component, a vertical field was not required to obtain a good fit in any of the rings in either galaxy. Polarization angles at $\lambda 3.5$ cm and $\lambda 6.2$ cm were averaged in sectors with an opening angle of 10° in NGC 1097 and 20° in NGC 1365. The greater of the standard deviation and the noise within a sector was taken as the error in polarization angle.

The regular magnetic field is modelled as

$$\begin{aligned}
B_r &= R_0 \sin p_0 + R_1 \sin p_1 \cos(\phi - \beta_1) \\
&\quad + R_2 \sin p_2 \cos(2\phi - \beta_2), \\
B_\phi &= R_0 \cos p_0 + R_1 \cos p_1 \cos(\phi - \beta_1) \\
&\quad + R_2 \cos p_2 \cos(2\phi - \beta_2), \\
B_z &= R_{z0} + R_{z1} \cos(\phi - \beta_{z1}) + R_{z2} \cos(2\phi - \beta_{z2}),
\end{aligned} \tag{B.1}$$

where R_i is the amplitude of the i 'th mode in units of rad m^{-2} , p_i is its pitch angle and β_i determines the azimuth where the corresponding non-axisymmetric mode is maximum. The magnetic field in each non-axisymmetric mode of this model is approximated by a logarithmic spiral, $p_i = \text{const}$, within a given ring. However, the superposition of such modes is not restricted to represent a logarithmic spiral. For further details of the method, see Berkhuijsen et al. (1997) and Fletcher et al. (2004).

The foreground Faraday rotation due to the magnetic field of the Milky Way was neglected in all cases, since both galaxies lie far from the Galactic plane; the expected (but unknown) contribution of the Milky Way to RM in the direction of the two galaxies is about 10 rad m^{-2} and will not significantly affect the fits. S is the residual of the fit and the appropriate χ^2 value, at the 95% confidence

level, is shown for the number of fit parameters and data points. A fit is statistically acceptable if $S \leq \chi^2$. The χ^2 values vary from ring to ring (even when the same number of fit parameters are used) as some sectors are excluded from the model, either because the average measured signal is too weak or because the sector represents a clear outlier from the global pattern.

References

- Athanassoula, E. 1992a, MNRAS, 259, 328
Athanassoula, E. 1992b, MNRAS, 259, 345
Balbus, S. A., & Hawley, J. F. 1998, Rev. Mod. Phys., 70, 1
Barth, A. J., Ho, L. C., Filippenko, A. V., & Sargent, W. L. 1995, AJ, 110, 1009
Beck, R., in Cosmic Magnetic Fields, eds. R. Wielebinski & R. Beck (Heidelberg: Springer), p. 41
Beck, R., & Krause, M. 2005, AN, 326, 414
Beck, R., Brandenburg, A., Moss, D., Shukurov, A., & Sokoloff, D. 1996, ARAA, 34, 155
Beck, R., Ehle, M., Shoutenkov, V., Shukurov, A., & Sokoloff, D. 1999, Nature, 397, 324
Beck, R., Shoutenkov, V., Ehle, M., et al. 2002, A&A, 391, 83
Beck, R., Ehle, M., Fletcher, A., et al. 2005, in The Evolution of Starbursts, Proc. 331st Heraeus Seminar, eds. S. Hüttemeister et al., AIP Conf. Proc., 783, 216
Bergin, E. A., Hartmann, L. W., Raymond, J. C. & Ballesteros-Paredes, J. 2004, ApJ, 612, 921
Berkhuijsen, E. M., Horellou, C., Krause, M., Neininger, N., Poezd, A. D., Shukurov, A., & Sokoloff, D. D. 1997, A&A, 318, 700
Chiba, M., & Lesch, H. 1994, A&A, 284, 731
Crosthwaite, L. P. 2001, PhD Thesis, Univ. California
Ehle, M., & Beck, R. 1993, A&A, 273, 45
Ehle, M., Pietsch, W., Beck, R., Klein, U. 1998, A&A, 329, 39
Elmegreen, B. G. 1994, ApJ, 425, L73
Englmaier, P., & Gerhard, O. 1997, MNRAS, 287, 57
Fletcher, A., & Shukurov, A. 2005, in preparation
Fletcher, A., Berkhuijsen, E. M., Beck, R., & Shukurov, A. 2004, A&A, 414, 53
Gerin, M., Nakai, N., & Combes, F. 1988, A&A, 203, 44
Greenawalt, B., Walterbos, R. A. M., Thilker, D., & Hoopes, C. G. 1998, ApJ, 506, 135
Harnett, J., Ehle, M., Fletcher, A., et al. 2004, A&A, 421, 571
Hummel, E., van der Hulst, J. M., & Keel, W. C. 1987, A&A, 172, 32
Jörsäter, S., & van Moorsel, G. A. 1995, AJ, 110, 2037
Jura, M. 1975, ApJ, 197, 575
Knapen, J. 2004, in Penetrating Bars through Masks of Cosmic Dust, eds. D. L. Block et al. (Dordrecht: Kluwer), Astr. & Sp. Sc. Library, 319, 189
Kohno, K., Ishizuki, S., Matsushita, S., Vila-Vilaró, B., & Kawabe, R. 2003, PASJ, 55, L1
Lindblad, P. O. 1999, A&AR, 9, 221
Lindblad, P. A. B., Lindblad, P. O., & Athanassoula, E. 1996, A&A, 313, 65
Maciejewski, W., Teuben, J., Sparke, L. S., & Stone, J. M. 2002, MNRAS, 329, 502
Mestel, L. & Strittmatter, P. A. 1967, MNRAS, 137, 95
Moss, D. 1998, MNRAS, 297, 860
Moss, D., Korpi, M., Rautiainen, P., & Salo, H. 1998, A&A, 329, 895

Table B.1. Parameters of fitted model for NGC 1097, with notation as in Eq. B.1

	Ring	$1.25 < r < 2.5 \text{ kpc}$	$1.25 < r < 2.5 \text{ kpc}$	$2.5 < r < 3.75 \text{ kpc}$	$2.5 < r < 3.75 \text{ kpc}$	$3.75 < r < 5 \text{ kpc}$
	Azimuth	$20^\circ \leq \phi \leq 190^\circ$	$200^\circ \leq \phi \leq 370^\circ$	$20^\circ \leq \phi \leq 190^\circ$	$200^\circ \leq \phi \leq 370^\circ$	$0^\circ \leq \phi \leq 350^\circ$
R_0	rad m ⁻²	-169 ± 30	55^{+44}_{-7}	-126^{+33}_{-44}	-57 ± 14	-155 ± 8
p_0	deg	41 ± 2	27 ± 2	36 ± 4	35 ± 6	23 ± 2
R_1	rad m ⁻²				43 ± 12	-51 ± 7
p_1	deg				131 ± 22	82 ± 16
β_1	deg				-105 ± 10	82 ± 5
R_2	rad m ⁻²	-339^{+44}_{-52}	48^{+7}_{-61}	45 ± 24		75 ± 7
p_2	deg	40 ± 2	-153 ± 2	13^{+16}_{-24}		3 ± 4
β_2	deg	-25 ± 3	-21 ± 41	12 ± 15		5 ± 5
S		38	37	40	33	74
χ^2		44	45	47	45	78

Table B.2. Parameters of fitted model for NGC 1365, with notation as in Eq. B.1 and ring width 1.75 kpc.

		Ring centre (kpc)						
		3.50	5.25	7.00	8.75	10.50	12.25	14.00
R_0	rad m ⁻²	55 ± 3	65 ± 2	52 ± 6	100 ± 1	90^{+18}_{-1}	56 ± 14	32 ± 6
p_0	deg	34 ± 2	17 ± 1	31 ± 1	22 ± 1	37^{+1}_{-6}	29 ± 11	33 ± 6
R_1	rad m ⁻²	-69 ± 4	-112 ± 2		-142 ± 3	-56^{+13}_{-1}	13 ± 17	8 ± 4
p_1	deg	23 ± 3	11 ± 1		21 ± 1	-21^{+1}_{-31}	74^{+133}_{-65}	-90^{+42}_{-52}
β_1	deg	-118^{+8}_{-1}	-108 ± 1		266 ± 1	-58^{+1}_{-13}	-290 ± 50	-38^{+43}_{-30}
R_2	rad m ⁻²	32 ± 6	85 ± 4	-53 ± 6	-64 ± 2	62^{+1}_{-30}	-65 ± 16	32 ± 5
p_2	deg	41 ± 4	18 ± 2	-148 ± 2	25 ± 2	-131^{+9}_{-1}	56 ± 22	-114 ± 14
β_2	deg	39 ± 4	11 ± 1	21 ± 3	-9 ± 2	0^{+11}_{-1}	-14 ± 6	-11 ± 5
S		29	32	35	34	18	23	20
χ^2		34	33	43	36	22	33	22

Moss, D., Shukurov, A., & Sokoloff, D. 2000, A&A, 358, 1142
Moss, D., Shukurov, A., Sokoloff, D., Beck, R., & Fletcher, A. 2001, A&A, 380, 55
Moss, D., Englmaier, P., Shukurov, A., Snodin, A., Beck, R., & Sokoloff, D. D. 2005, A&A, in prep.
Nulsen, P. E. J., Stewart, G. C., Fabian, A. C. 1984, MNRAS, 208, 185
Ondrechen, M. P. 1985, AJ, 90, 1474
Ondrechen, M. P., & van der Hulst, J. M. 1983, ApJ, 269, L47
Ondrechen, M. P., & van der Hulst, J. M. 1989, ApJ, 342, 29
Ondrechen, M. P., van der Hulst, J. M., & Hummel, E. 1989, ApJ, 342, 39
Otmianowska-Mazur, K., von Linden, S., Lesch, H., & Skupniewicz, G. 1997, A&A, 323, 56
Pérez-Olea, D. E., & Colina, L. 1996, ApJ, 468, 191
Pfeffermann, E., Briel, U. G., Hippmann, H., et al. 1987, Proc. SPIE, 33, 519
Piner, B. G., Stone, J. M., & Teuben, P. J. 1995, ApJ, 449, 508

Prieto, M. A., Maciejewski, W., & Reunanen, J. 2005, AJ, 130, 1472
Quillen, A. C., Frogel, J. A., Kuchinski, L. E., & Terndrup, D. M. 1995, AJ, 110, 156
Raymond, J. C., Cox, D. P., Smith, B. W. 1976, ApJ, 204, 290
Raymond, J. C., Smith, B. W. 1977, ApJS, 35, 419
Reynaud, D., & Downes, D. 1998, A&A, 337, 671
Reynolds, R. J. 1990, ApJ, 349, L17
Roberts, W. W., Huntley, J. M., & van Albada, G. D. 1979, ApJ, 233, 67
Roussel, H., Vigroux, L., Bosma, A., et al. 2001, A&A, 369, 473
Sanqvist, A., Jörsäter, S., & Lindblad, P. O. 1995, A&A, 295, 585
Sheth, K., Vogel, S. N., Regan, M. W., et al. 2002, AJ, 124, 2581

- Sokoloff, D. D., Bykov, A. A., Shukurov, A., Berkhuijsen,
E. M., Beck R., & Poezd, A. D. 1998, MNRAS, 299, 189,
and MNRAS, 303, 207 (Erratum)
- Syer, D., & Narayan, R. 1993, MNRAS, 262, 749
- Zimmermann, H. U., Boese, G., Becker, W., Belloni, T., et al.
1998, *EXSAS User's Guide*, MPE Report

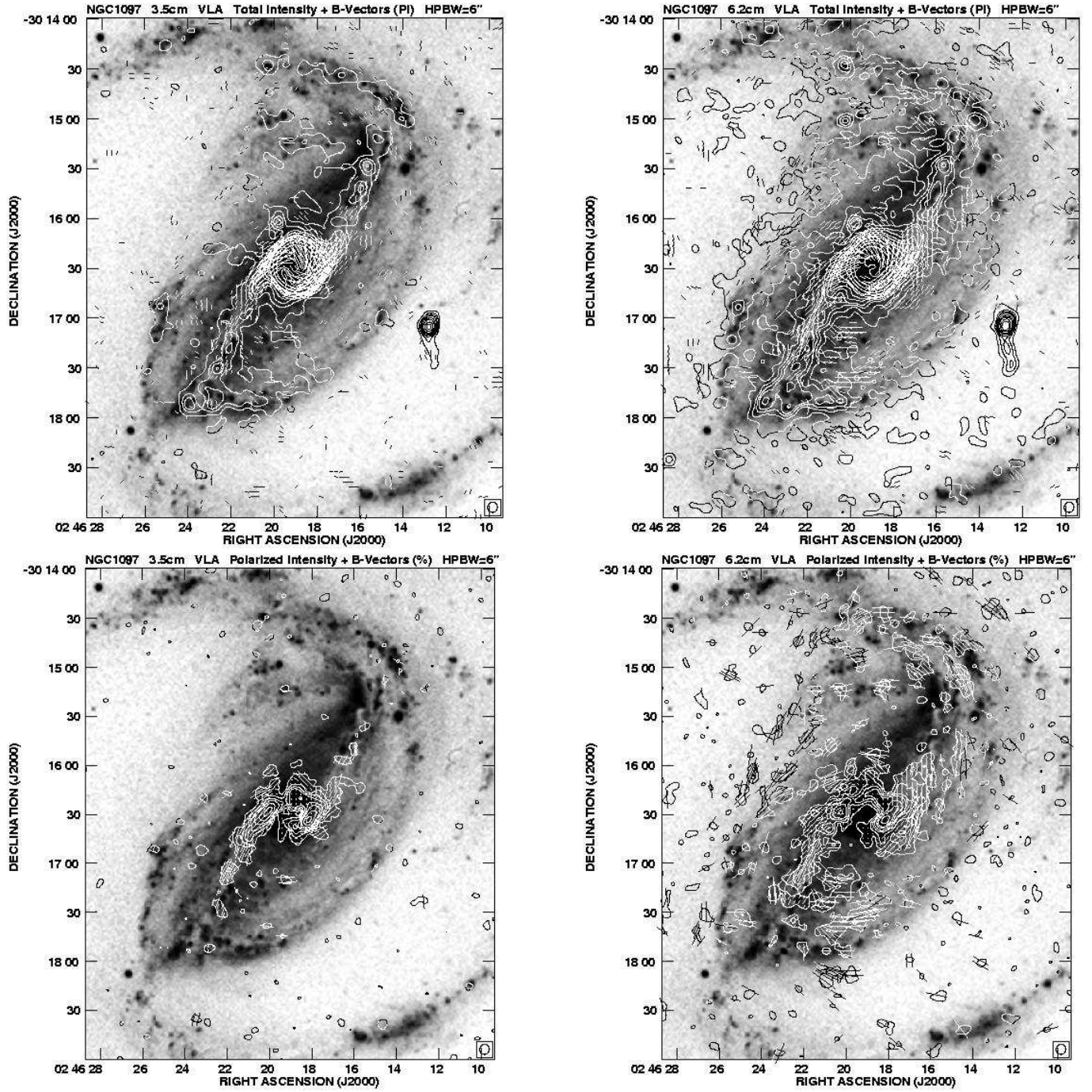


Fig. 1. *Top row:* Total intensity contours and observed B -vectors ($E+90^\circ$) of NGC 1097 at $\lambda 3.5$ cm (left) and $\lambda 6.2$ cm (right) at $6''$ resolution. The contour intervals are 1, 2, 3, 4, 6, 8, 12, 16, 32, 64, 128 times $40 \mu\text{Jy}/\text{beam area}$. The vector length is proportional to polarized intensity, $3''$ length corresponds to $20 \mu\text{Jy}/\text{beam area}$. The vector orientations are not corrected for Faraday rotation. The background optical image was kindly provided by Halton Arp. *Bottom row:* Polarized intensity contours and observed B -vectors at $\lambda 3.5$ cm (left) and $\lambda 6.2$ cm (right) at $6''$ resolution. The vector length is proportional to fractional polarization, $3''$ length corresponds to 20%. The contour intervals are 1, 2, 3, 4, 6, 8, 12, 16 times $20 \mu\text{Jy}/\text{beam area}$. The vector orientations are not corrected for Faraday rotation. Here and in other maps, the beam size is shown in the bottom right corner of each panel.

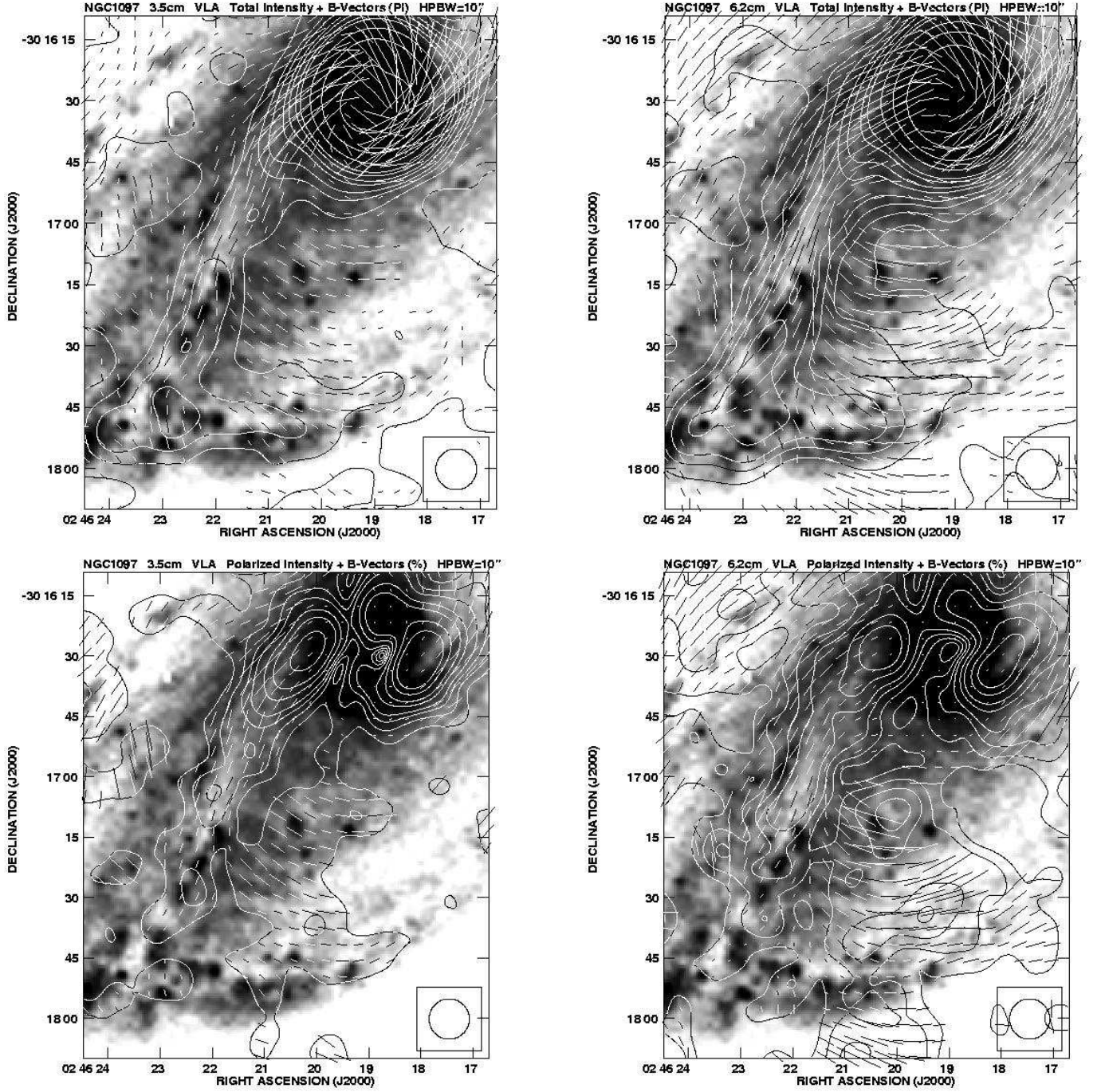


Fig. 2. *Top row:* Total intensity contours and observed B -vectors ($E + 90^\circ$) of the central and southern parts of NGC 1097 at $\lambda 3.5$ cm (left) and $\lambda 6.2$ cm (right) at $10''$ resolution. The contour intervals are as in Fig. 1, with the lowest contour level at $80 \mu\text{Jy}/\text{beam area}$. The vector length is proportional to polarized intensity, $3''$ length corresponds to $30 \mu\text{Jy}/\text{beam area}$. The vector orientations are not corrected for Faraday rotation. *Bottom row:* Polarized intensity contours and observed B -vectors at $\lambda 3.5$ cm (left) and $\lambda 6.2$ cm (right) at $10''$ resolution. The contour intervals are as in Fig. 1, with the lowest contour level at $20 \mu\text{Jy}/\text{beam area}$. The vector length is proportional to fractional polarization, $3''$ length corresponds to 20% . The vector orientations are not corrected for Faraday rotation.

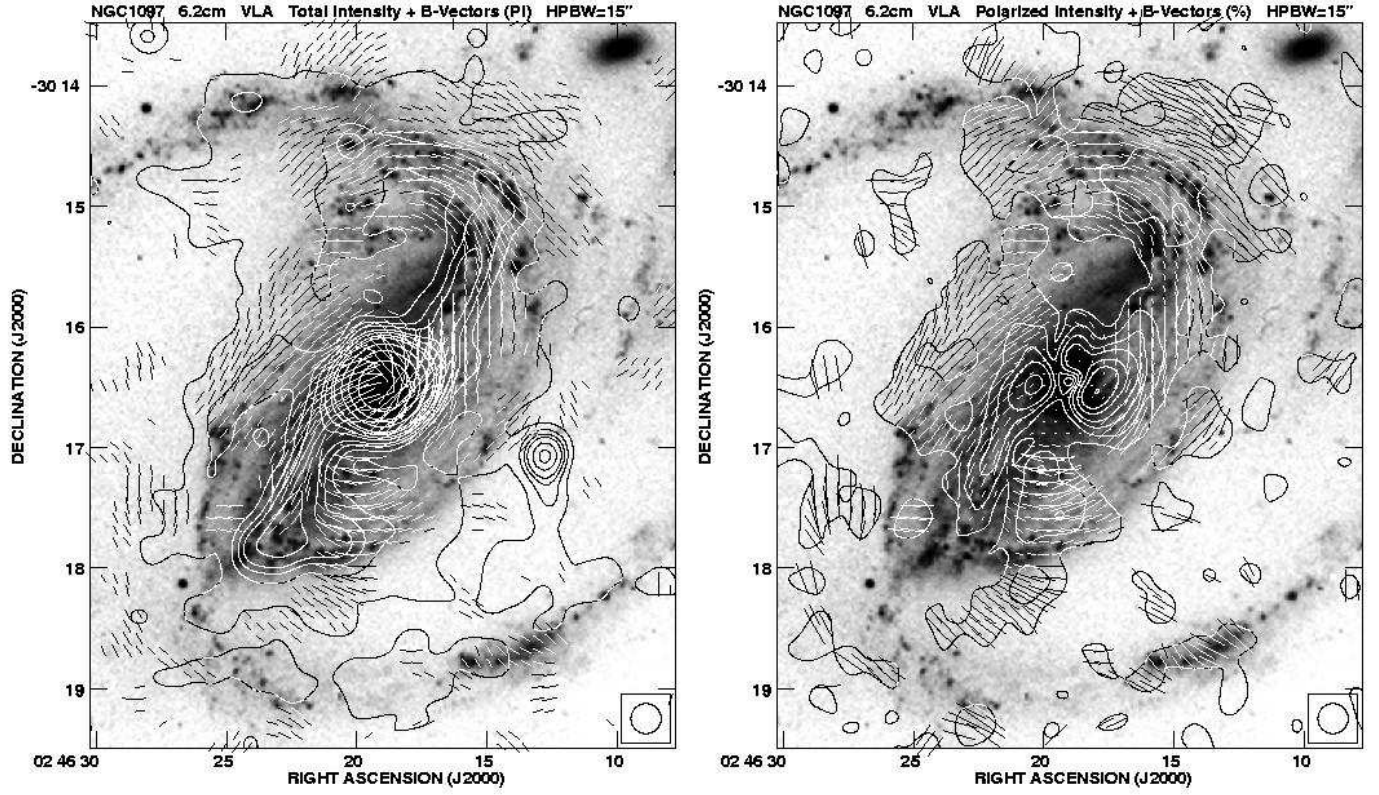


Fig. 3. *Left:* Total intensity contours and observed B -vectors ($E + 90^\circ$) of NGC 1097 at $\lambda 6.2$ cm at $15''$ resolution. The contour intervals are as in Fig. 1, with the lowest contour level at $150 \mu\text{Jy}/\text{beam area}$. The vector length is proportional to polarized intensity, $3''$ length corresponds to $30 \mu\text{Jy}/\text{beam area}$. The vector orientations are not corrected for Faraday rotation. The companion galaxy NGC 1097A is visible in the top right corner. *Right:* Polarized intensity contours and observed B -vectors at $15''$ resolution. The vector length is proportional to fractional polarization, $3''$ length corresponds to 10% . The contour intervals are as in Fig. 1, with the basic contour level at $50 \mu\text{Jy}/\text{beam area}$. The vector orientations are not corrected for Faraday rotation.

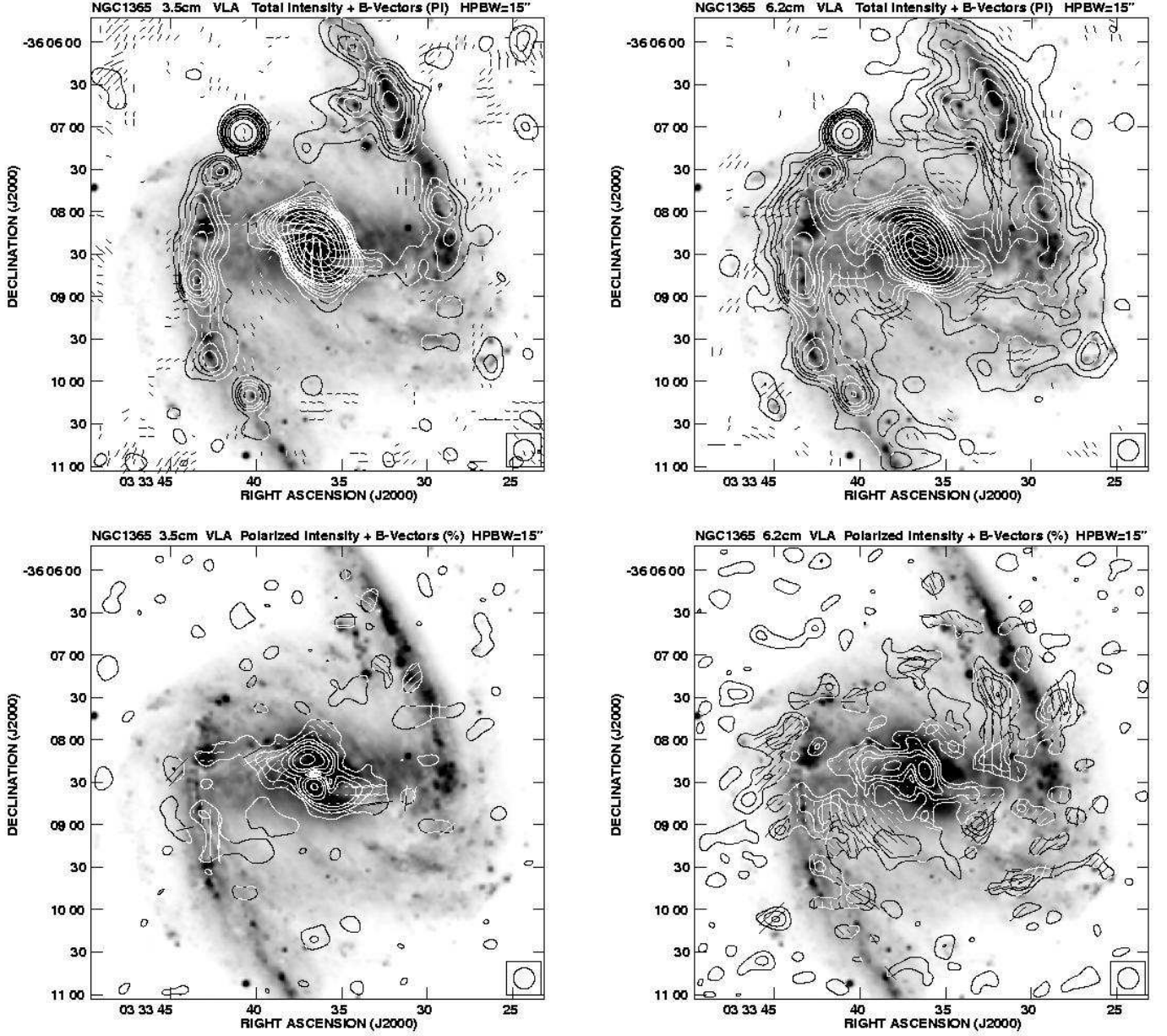


Fig. 4. *Top row:* Total intensity contours (corrected for primary beam attenuation) and observed B -vectors ($E + 90^\circ$) of NGC 1365 at $\lambda 3.5$ cm (left) and $\lambda 6.2$ cm (right) at $15''$ resolution. The contour intervals are 1, 2, 3, 4, 6, 8, 12, 16, 32, 64, 128, 256, 512 times $60 \mu\text{Jy}/\text{beam area}$. The vector length is proportional to polarized intensity, $3''$ length corresponds to $30 \mu\text{Jy}/\text{beam area}$. The vector orientations are not corrected for Faraday rotation. The background optical *ESO* image was kindly provided by Per Olof Lindblad. *Bottom row:* Polarized intensity contours and observed B -vectors at $\lambda 3.5$ cm (left) and $\lambda 6.2$ cm (right) at $15''$ resolution. The contour intervals are 1, 2, 3, 4, 6, 8, 12 times $25 \mu\text{Jy}/\text{beam area}$. The vector length is proportional to fractional polarization, $3''$ length corresponds to 10%. The vector orientations are not corrected for Faraday rotation.

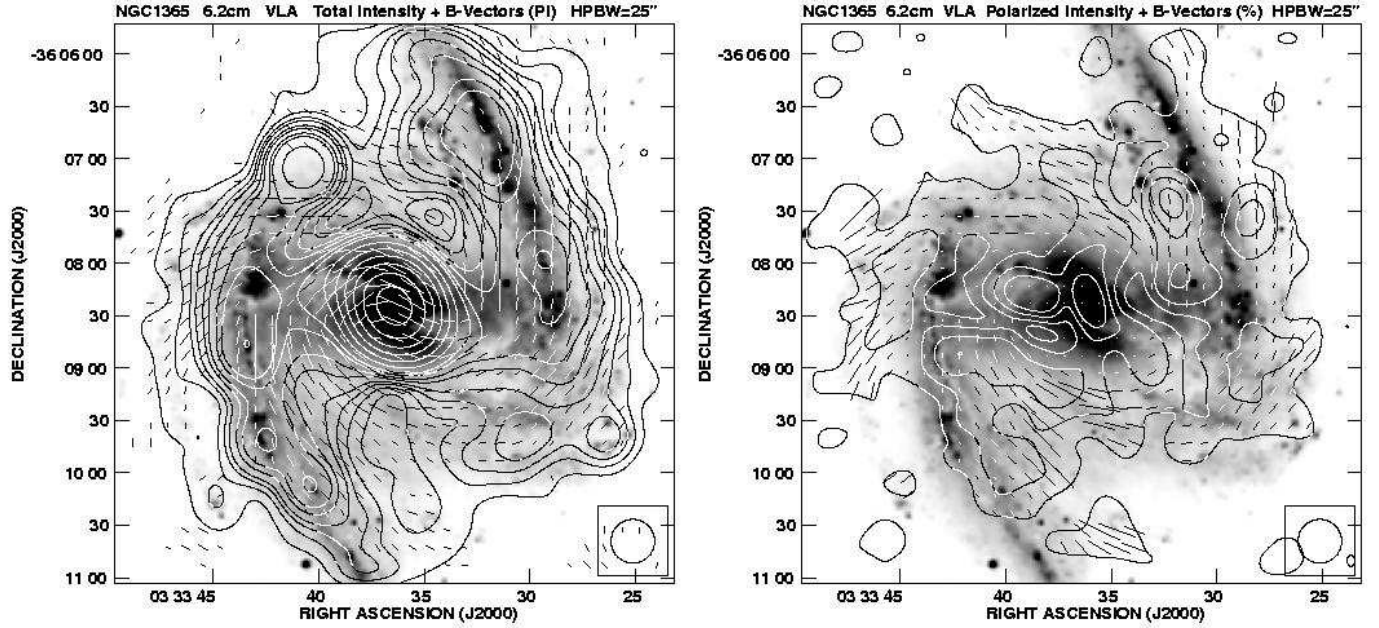


Fig. 5. *Left:* Total intensity contours (corrected for primary beam attenuation) and observed B -vectors ($E + 90^\circ$) of NGC 1365 at $\lambda 6.2$ cm at $25''$ resolution. The contour intervals are as in Fig. 4, with the lowest contour level at $80 \mu\text{Jy}/\text{beam area}$. The vector length is proportional to polarized intensity, $3''$ length corresponds to $30 \mu\text{Jy}/\text{beam area}$. The vector orientations are not corrected for Faraday rotation. *Right:* Polarized intensity contours and observed B -vectors at $25''$ resolution. The contour intervals are as in Fig. 4, with the basic contour level at $40 \mu\text{Jy}/\text{beam area}$. The vector length is proportional to fractional polarization, $3''$ length corresponds to 10% . The vector orientations are not corrected for Faraday rotation.

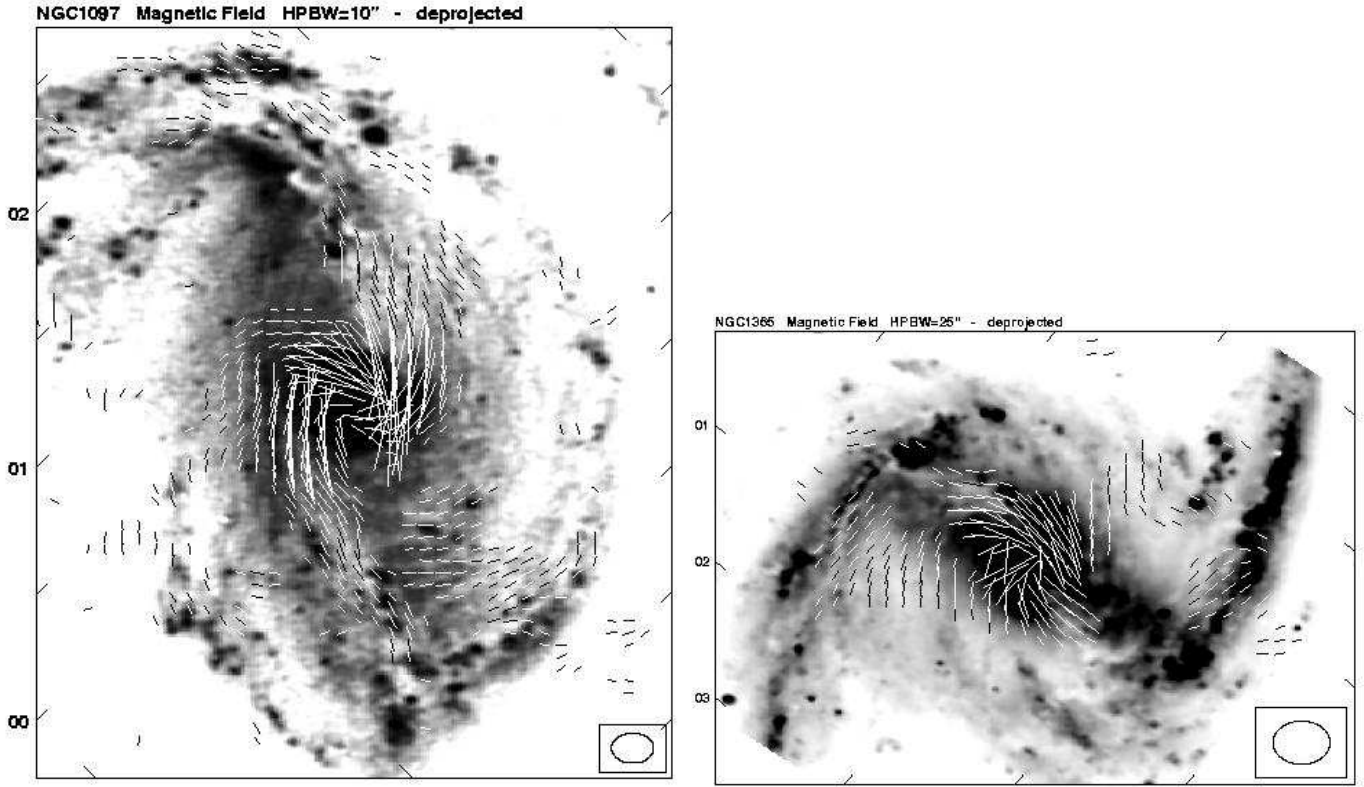


Fig. 10. Intrinsic orientation of the magnetic field B_P (regular and/or anisotropic random), obtained from polarized synchrotron emission in NGC 1097 (left) and NGC 1365 (right), corrected for Faraday rotation and deprojected into the galaxies' planes, with the major axis oriented north-south. The vector length is proportional to polarized intensity at $\lambda 3.5$ cm. The resolutions are $10''$ and $25''$, respectively; the deprojected beam is shown in the lower right corner. North is at top left and top right of the NGC 1097 and NGC 1365 images, respectively. Distances given in axis labels are in arcmin.

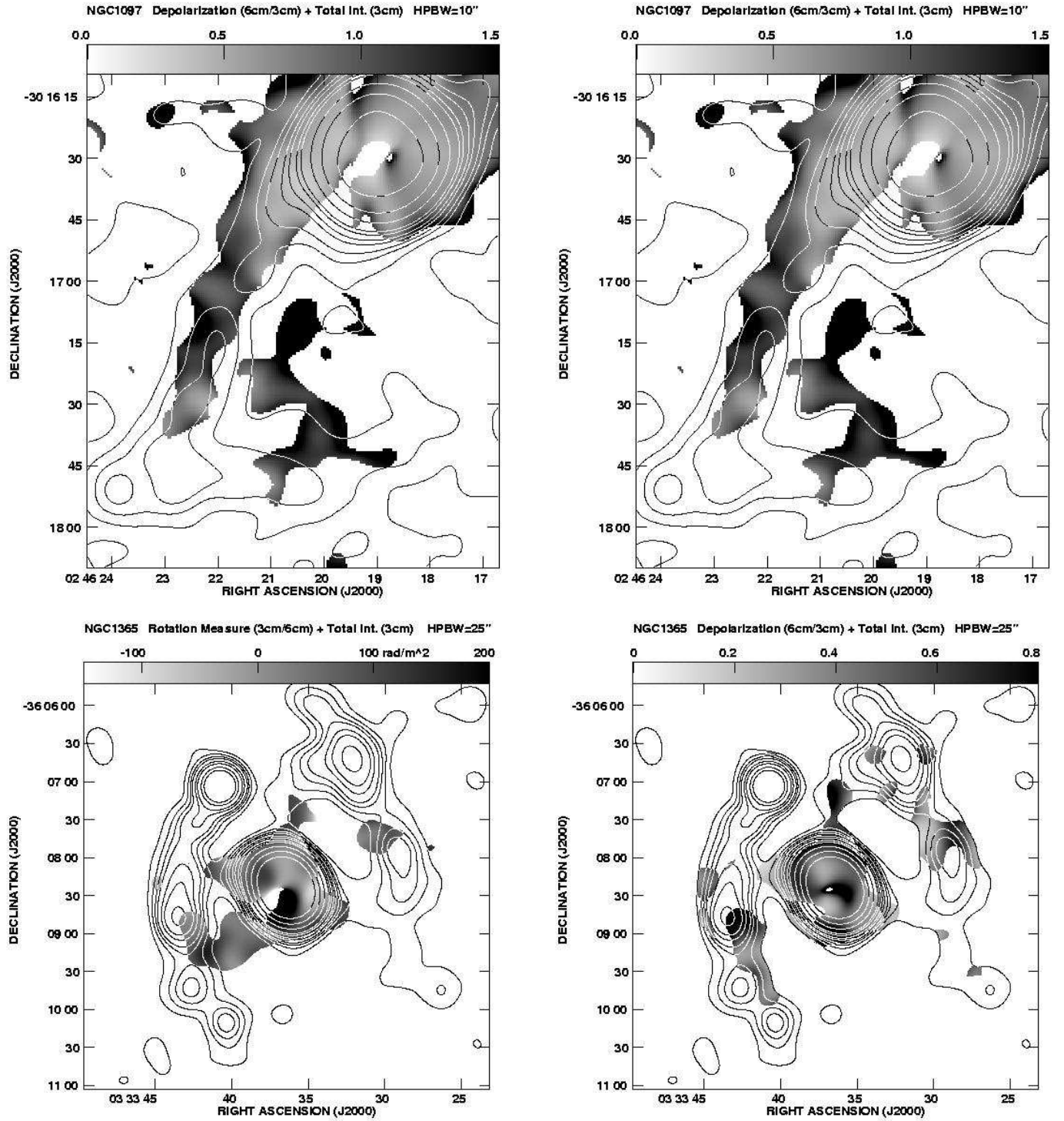


Fig. 11. *Top row:* Faraday rotation measure (left) and Faraday depolarization (right) of NGC 1097 in grey scales between $\lambda 3.5$ cm and $\lambda 6.2$ cm at $10''$ resolution, overlaid onto contours of total intensity at $\lambda 3.5$ cm. *Bottom row:* Faraday rotation measure (left) and Faraday depolarization (right) of NGC 1365 in grey scales at $25''$ resolution, overlaid onto contours of total intensity at $\lambda 3.5$ cm.

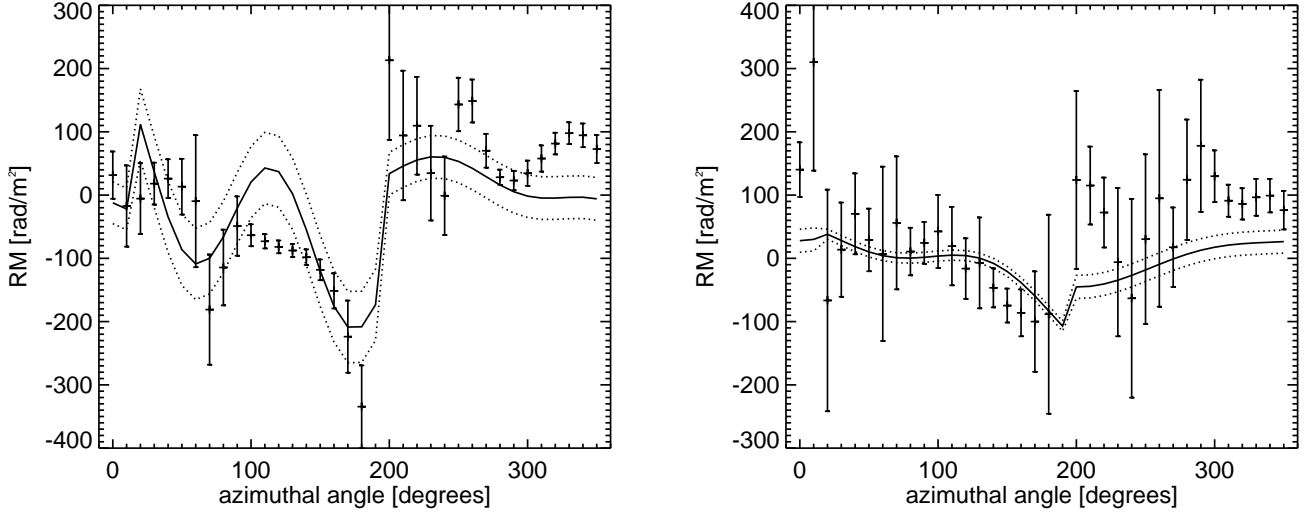


Fig. 12. The azimuthal variation of RM in NGC 1097, obtained between $\lambda 3.5$ cm and $\lambda 6.2$ cm at $10''$ resolution in the rings $1.25 < r < 2.5$ kpc ($15''$ – $30''$, left) and $2.5 < r < 3.75$ kpc ($30''$ – $45''$, right) where r is the radius from the centre of NGC 1097. The error bars show the standard deviation of RM in each sector. Solid lines are RM values obtained from the fits to polarization angles described in Sect. 4, with the dotted lines showing the range of RM. The azimuthal angle is measured in the galaxy's plane (position angle of the major axis of -45° , inclination of 45°) counterclockwise from the northern major axis. The southern ridge line of polarized intensity is located at 130° azimuthal angle (left) and at 160° (right).

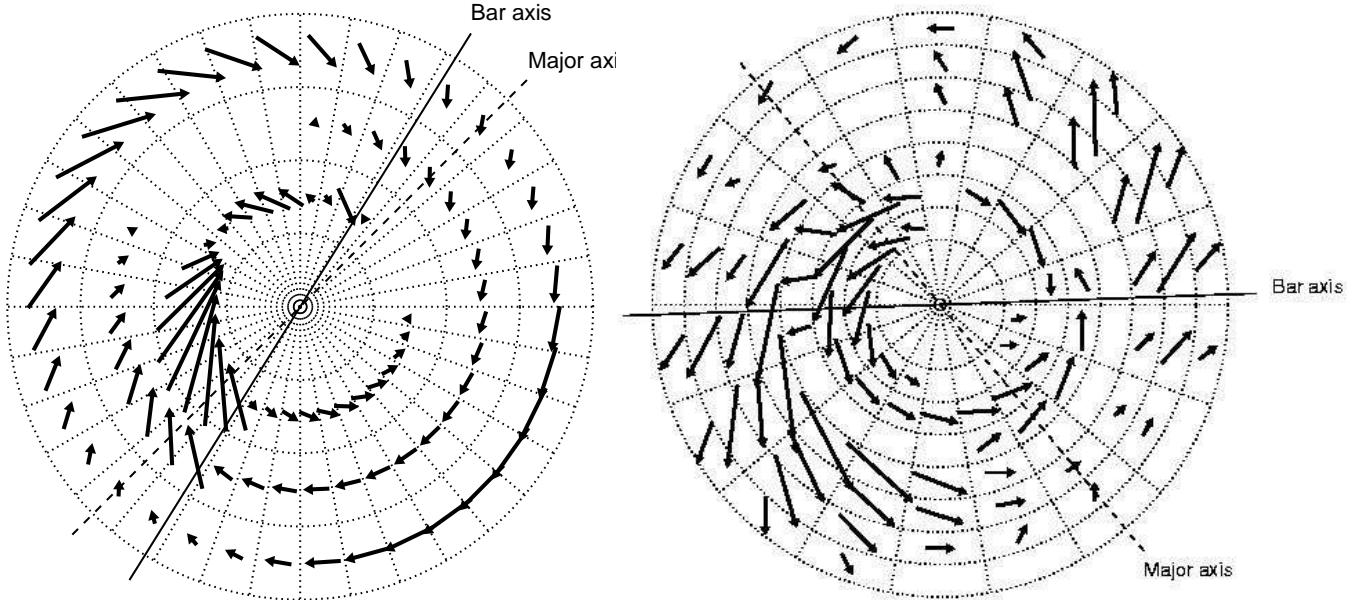


Fig. 13. The global structure of the regular magnetic field in NGC 1097 (left) and NGC 1365 (right). Both plots are face-on views of the modelled galaxy, with the major axis shown by a dashed line and the bar axis by a solid line. The ring boundaries for NGC 1097 are at $r = 1.25$, 2.5 , and 3.75 kpc, covering the inner and mid-bar, where the half-length of the bar is $\simeq 10$ kpc. The NGC 1365 rings are centred at $r = 3.5$, 5.25 , 7.0 , 8.75 , 10.5 , 12.25 and 14 kpc, with a half-length of the bar of $r \simeq 11$ kpc. In both figures, the vector lengths are proportional to the modelled Faraday rotation measure in a sector and are only shown where $RM > 20 \text{ rad m}^{-2}$. The vectors in the outer ring of NGC 1097 are scaled up by a factor 1.5 compared to those of the inner ring, the vectors for NGC 1365 all have the same scaling.

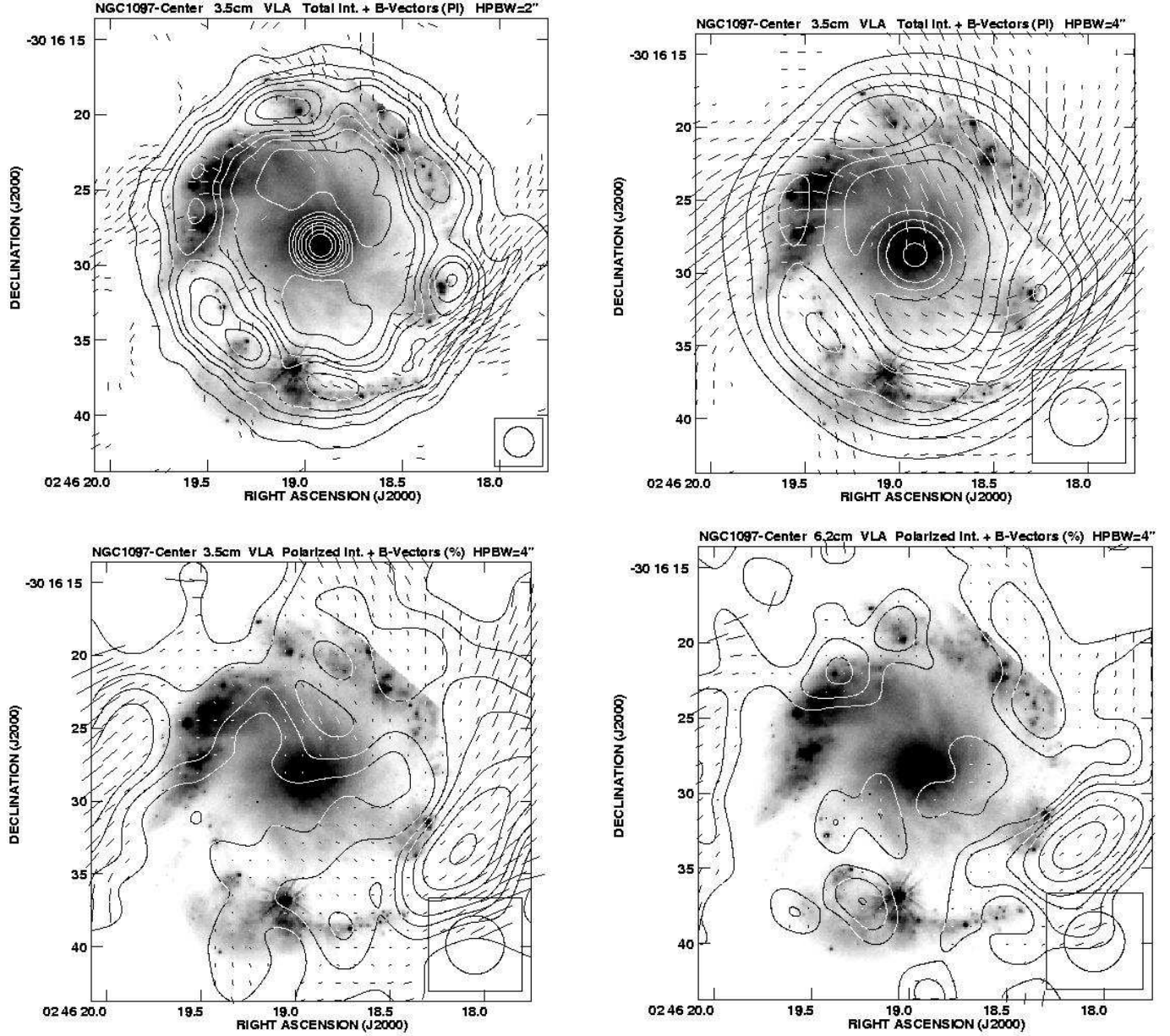


Fig. 14. *Top row:* Total intensity contours and observed B -vectors ($E + 90^\circ$) in the circumnuclear ring of NGC 1097 at $\lambda 3.5$ cm at 2" (left) and 4" (right) resolutions. The contour levels are 1, 2, 3, 4, 6, 8, 12, 16, 32, 64, 128 times the basic contour level, which is 150 and 600 $\mu\text{Jy}/\text{beam area}$, in the left- and right-hand panels, respectively. The vector length is proportional to polarized intensity, 1" length corresponds to 50 $\mu\text{Jy}/\text{beam area}$. The vector orientations are not corrected for Faraday rotation. The background optical V-band *HST* image was kindly provided by Aaron Barth. *Bottom row:* Polarized intensity contours and observed B -vectors at $\lambda 3.5$ cm (left) and $\lambda 6.2$ cm (right) at 4" resolution. The vector length is proportional to fractional polarization, 1" length corresponds to 17%. The contour levels are 1, 2, 3, 4, 6, 8, 12 times 20 $\mu\text{Jy}/\text{beam area}$. The vector orientations are not corrected for Faraday rotation.

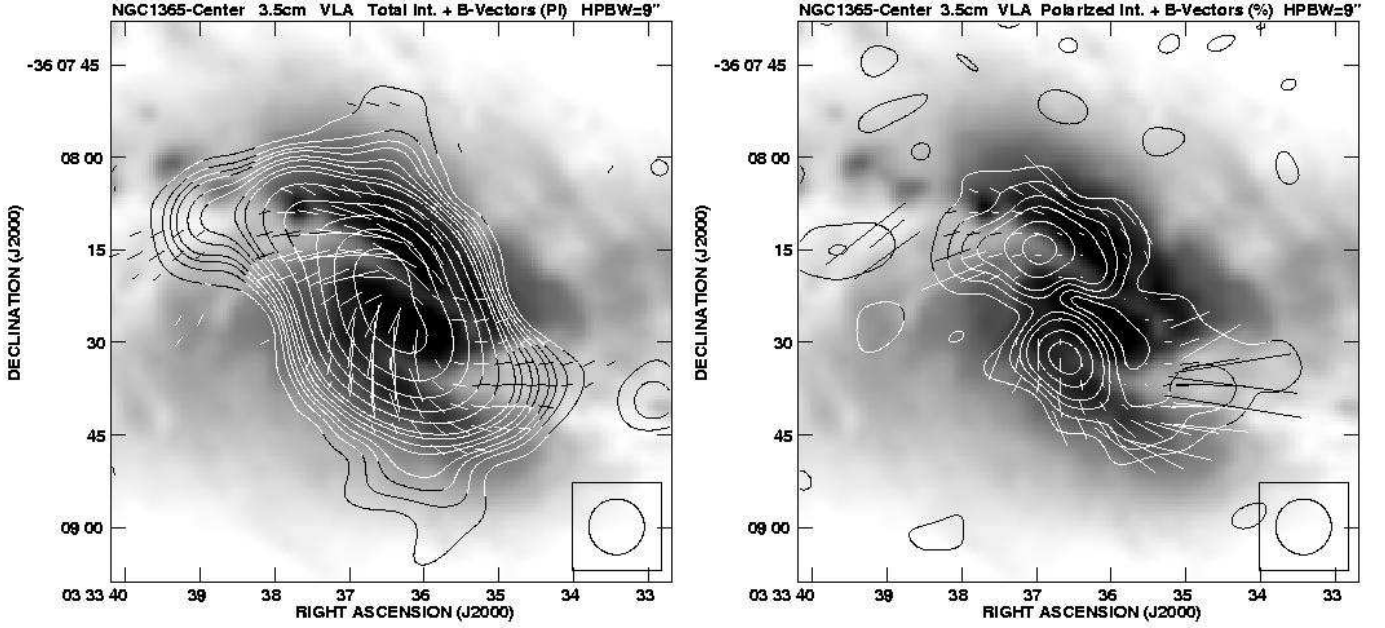


Fig. 15. *Left:* Total intensity contours and observed B -vectors ($E + 90^\circ$) in the central region of NGC 1365 at $\lambda 3.5$ cm at $9''$ resolution. The contour intervals are 1, 2, 3, 4, 6, 8, 12, 16, 32, 64, 128, 256, 512 times $40 \mu\text{Jy}/\text{beam area}$. The vector length is proportional to polarized intensity, $1''$ length corresponds to $20 \mu\text{Jy}/\text{beam area}$. The vector orientations are not corrected for Faraday rotation. *Right:* Polarized intensity intensity contours and observed B -vectors ($E + 90^\circ$) of NGC 1097 at $\lambda 3.5$ cm at $9''$ resolution. The contour intervals are 1, 2, 3, 4, 6, 8 times $30 \mu\text{Jy}/\text{beam area}$. The vector length is proportional to fractional polarization, $1''$ length corresponds to 1.7%. – The vector orientations are not corrected for Faraday rotation.

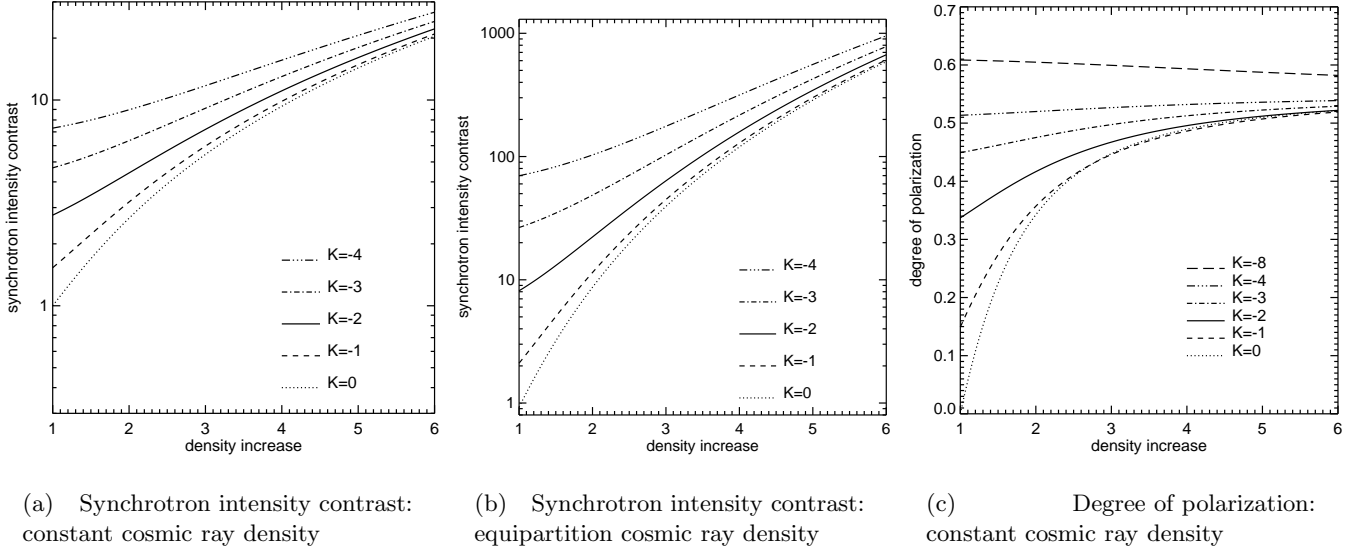


Fig. 21. The changes in total intensity and degree of polarization arising from a sheared and compressed, initially isotropic, random magnetic field as a function of the gas density contrast ϵ_ρ in a shock for the geometry of the galaxy NGC 1365. **(a):** The increase in total synchrotron intensity in the case of constant cosmic ray density, Eq. (A.6). **(b):** The increase in total synchrotron intensity in the case of energy density equipartition between the magnetic field and cosmic rays, Eq. (A.7). **(c):** The degree of polarization in the case of constant cosmic ray density, Eq. (A.8), with $p_0 = 0.7$. The parameter $K = \Delta V_r l / (c_s d)$ is the ratio of the turbulent eddy turnover timescale l/c_s to the shearing timescale $d/\Delta V_r$ and is the appropriate measure of the strength of the shearing; high $|K|$ means strong shear. The model inclination is $i = 40^\circ$ and the position angle of the shock is $\phi = 40^\circ$, the parameters of NGC 1365.